Lund University

Master Thesis in Physics

Single Ion Detection of Cerium in Y_2SiO_5 microcrystals

Vassily Kornienko

Supervisor: Stefan Kröll

LUND UNIVERSITY
Faculty of Science

Department of Atomic Physics

Hand-in date: 16th December 2018
Project Duration: August 2017 - December 2018

Popular Science Article

Imagine an orchestra of professional musicians. They can read any set of notes that is presented to them and upon hearing the other musicians of the orchestra, will play their part in the correct volume and style. Furthermore, they all follow an identical 'clock' meaning that they all feel the same beat. They will even slow down or increase in speed all in sync. These musicians are also so skilled that even if there is a note missing in the score they are given, they will just know what to play, since it will follow naturally from the rest of the piece. Some more skillful musicians might even decide to add little details to the score that are not even written.

Now say that I, a non-musical person, somehow manage to sit down and write a really complicated piece of music. I probably do this with the help of some mathematical formula and a computer. There is however a problem, one note is missing and there is no way, for the life of me, that I can figure out what that note is supposed to be. I decide to give it to the orchestra, let them play the score and try to listen for the missing note that one of the members will play. We have already secured that this member will play the missing note without a second thought, because it just naturally fits in with the rest of the piece.

However, when the orchestra starts playing and the time has come for the missing note to be played, the noise from all the other musicians will overshadow the sound coming from the musician who is supposed to play the missing note. Even after retrying hundreds of times, I cannot with certainty say what the missing note is, there is simply too much noise.

How can I find out what the missing note is? There are two possibilities:

1. I can ask the musician to play that note much louder than it is being played at the moment. Unfortunately upon hearing this loud note, the whole orchestra will collapse because the higher volume of the note will not flow with the rest of the score.

2. I could sit right next to the musician that is to play the missing note and listen very carefully. However, I will be a distraction to the musician and the rest of the orchestra so they will not even be able to start playing the piece.

A possibility that could work is to add another 'infiltrator' musician that can sit next to the person playing the missing note, remember it and then report it to me after the score has been played. That way, since the infiltrator is a musician, he/she will not gain attention from the others and also will remember the note that was played efficiently.

With this analogy in mind, imagine each musician is an atom that can be used as a quantum computer bit (qubit). With the assistance of laser pulses, each atom plays together in a quantum orchestra and we, the experimentalists, are looking for a certain unknown quantum state, or a note in the musician analogy. The infiltrator musician, or the link between us and the orchestra, will then correspond to a certain type of atom that interacts with the qubit atoms and us as the experimentalists. The link between the experimentalist and this infiltrator atom is where this thesis comes in, where I have worked on trying to detect a single atom in a crystal that contains billions. If this can be done, a very important milestone in quantum computing scheme pursued in Lund will be taken!

Abstract

Quantum computing with single instances of rare earth-ions doped into inorganic crystals shows great promise as a scalable design in the field of quantum information. A detectable and controllable single readout ion is necessary for the scheme proposed in Lund to work. Due to its short excited state lifetime and its cyclable 4f-5d transition, cerium has been deemed suitable for just this purpose. The approach taken in Lund for this single cerium detection is to use a homemade confocal microscopy setup. In previous work using this setup on bulk crystals, it has been assumed that the undetectability of single cerium is due to out of focus ions contributing to a noise floor that is higher than the fluorescence signal from a single one. Hence single ion detection is being attempted in microcrystals. This thesis outlines the process behind converting the confocal microscope into a microcrystal detection setup. Subsequently, Ce^{3+}:Y_2SiO_5 microcrystal spectroscopy experiments were performed. The energy level structure of cerium is reported to be identical to bulk, with a slight shift in wavelength, and the inhomogenous linewidth has proven to be inconclusive, although it hints towards being much wider than in bulk. Quantifying the homogenous linewidth of the cerium ions using Zeeman hole burning techniques was impervious to our attempts.

Contents

1 Introduction

The use of quantum mechanisms is what makes quantum computing considerably more efficient than classical computing at some specific problems. These mechanisms include entanglement, superposition states, and arbitrary unitary transformations, of which the latter greatly increases the variety of operations that can be performed beyond the classical logic gates. Exponential speed up can be achieved for Fourier transforms and large number factorization, an algorithm discovered by Peter Shor, while Grover's search algorithm provides a square-root speed up in the traveling salesman problem [1]. Furthermore, as thoroughly described on pages 204-212 of [2], a quantum simulation algorithm that can efficiently solve the time-dependent Schrödinger equation for a large variety of Hamiltonians can be implemented.

In order to perform these algorithms IBM's David P. DiVincenzo made a list of criteria that must be met by any physical realization of a quantum computer [3], widely used as a roadmap for quantum information laboratories. The list includes the requirement that it must be possible to prepare the individual entities, qubits, in precise ways followed by the ability to perform a universal set of unitary transformations. When it comes to actually achieving this experimentally, the balance between preserving the quantumness of the system while still requiring it to interact strongly with neighbouring systems, poses strong restraints on the type of scheme that can be used. As of today superconducting qubits and ion traps have come the farthest, while new ideas such as majorana qubits are being proposed [4].

One of the more relevant criteria to quantum computer implementations is that the system should be scalable to a reasonable number of qubits such that quantum algorithms can be performed. Due to error correcting necessities, the number of physical qubits needed to factorize a 2000 bit number is around 200×10^6 where 90% of them only perform error correction [5]! This poses extreme scalability demands on any system. Ions in ion traps have the problem that the entanglement between them becomes increasingly more complex as the number of qubits increases. Superconducting qubits on the other hand, are simply large objects (of the order of 1cm) that have to be held in dilution fridges that cannot go beyond a certain size. Ensemble qubits in rare-earth ion doped crystals, also scale very poorly due to the fact that each qubit consists of the order of 10^9 atoms, making it extremely difficult to find entangled pairs as one scales up the number of qubits. This is why it has been proposed to use single rare-earth ions doped in an inorganic crystal as qubits [6].

Rare-earth ion doped crystals are, as their name indicates, inorganic crystals that are doped with rare-earth atoms (atomic number 58 to 70 in the periodic table). A few of the most widely used crystals that are included in this group are yttrium orthosilicate, Y_2SiO_5 (YSO), used in this project, Yttrium Aluminum Garnet, $Y_3Al_5O_{12}$ (YAG), used widely in lasers, and Lithium Niobate, $LiNbO_3$, used as optical waveguides. Some of the extensively utilized rare earth ions are erbium, the atom of choice for all optical telecom communications, europium, an atom that is used as a red phosphor in televisions, and neodymium used for the famous Nd:YAG laser! It was previously believed that the rare-earths were created in supernova explosions, however, recent discoveries with LIGO, VIRGO and the plethora of telescopes used to look at a neutron-star merger, presents observational evidence that rare-earth atoms can in fact also be produced in these astronomical events [7] [8].

When a given rare-earth ion is doped into one of these crystals, the difference in radius

between the replaced atoms (yttrium for the case of YSO) and the dopant introduces a strain in the crystal lattice. This gives rise to a slightly different electric field surrounding for every dopant ion, causing their energy levels to shift a random amount in a random direction. This randomness gives rise to an inhomogenous spectral broadening of the dopant population in an analogous way as a gas of ions is inhomogenously broadened due to the Doppler effect. This broadening is normally in the range of 1 to 100 GHz.

Another property that these rare-earth dopants display is the fact that their valence electrons live in the 4f state. Consequently, electrons in the lower energy 5d state effectively create a faraday cage around these valence electrons, shielding them from outer electric field fluctuations (caused mainly by electric field fluctuations in the crystal lattice). Due to this shielding, these dopants have extremely long lifetimes, of the order of 100s of microseconds for the excited states and milliseconds to hours for the ground hyperfine energy levels. These long coherence times combined with short laser pulses gives rise to the possibility of attaining 10^4 optical operations before coherence is lost, a threshold that is essential to pass in order to perform efficient quantum operations, chapter 10 of [2].

These long lifetimes, corresponding to narrow spectral homogenous linewidths (Γ_h), along with the wide inhomogenous line (Γ_{ih}), allows for around Γ_{ih}/Γ_h frequency channels, where in each channel there will be a subset of the total population that can be uniquely addressed. This gives rise to many other applications such as high entendue spectral filters [9], slow light [10], frequency shifters [11] and high fidelity single qubit operations [12] [13].

The deep crystal potentials that the dopant ions experience, allows them to be close to each other despite the strong repelling force that is exerted between them. This spatial proximity entails that they can interact strongly via the dipole-dipole interaction. If one dopant is in the excited state its dipole moment changes, and the atoms surrounding it will experience a Stark shift of their energy levels. This can be used to efficiently entangle dopants to each other. Thus these atomic systems show great potential for being used as quantum computers.

If we are to use these properties within single instance quantum computation it is necessary to be able to detect and manipulate a single ion. This has already been performed for a variety of rare earths such as erbium in silicon nanophotonic structures [14], neodymium in yttrium orthovanadate using nanophotonic cavities [15] and praseodymium in YSO using a solid immersion lens [16]. As for cerium, the atom of choice here in Lund, a single ion has been detected in YAG [17], however, there is no clear way that would include this detection in a quantum computing protocol. This is where this thesis work comes in, namely detecting single cerium ions in YSO specifically for the use as a quantum state readout ion. With this, Section 2 will present and discuss some relevant background, Section 3 will present the equipment necessary for single ion detection, Section 4 will be about a simulation that was performed to understand the nature of the detection setup, Section 5 will show some experimental results that were obtained and the thesis will end with a short conclusion in Section 6.

2 Background

This section will include a short theoretical framework that gives meaning to this thesis project. For further reading there is a plethora of papers from the quantum information group that explains all aspects in great detail.

2.1 Spin-lattice coupling of a rare-earth ion in a crystal

The Hamiltonian describing an optically active center's spin-lattice coupling in a crystal (in our case a rare earth ion's spin-orbit levels coupled to the inorganic crystal's lattice) is given by the following equation (page 193 of [18]):

$$\hat{H} = \hat{H}_{FI}(r_i) + \hat{H}_c(r_i, R_l) + V(R_l) + \sum_l \frac{P_l^2}{2M_l}. \tag{1}$$

$\hat{H}_{FI}$ is the free ion Hamiltonian, $\hat{H}_c$ is the crystal field Hamiltonian, which depends on the position of the dopant ion, r_i and the positions of the crystal host ions R_l, V is the interatomic potential energy and the kinetic energy term corresponds to the kinetic energy of the crystal host atoms. The difficult term in Equation 1 is the crystal field Hamiltonian, where it is not obvious how to decouple the electronic motion of the dopant ion from the movement of the lattice atoms. This decoupling was first considered by Born and Oppenheimer in 1927, where it is argued that since the ionic motion is much slower than the electronic motion, the two can be decoupled. This way we can rather say that the electronic state 'adjusts' itself depending on the ionic position, or in mathematical terms, R_l can be regarded as a parameter rather than a variable.

The host crystal vibrations can be modeled as a 3-dimensional harmonic oscillator with phonons as the corresponding quanta. Hence the energy levels of a dopant ion within a crystal will be a sum of the free ion electronic levels, the crystal field electronic levels and the phonon levels. In order to aim for a certain electronic transition one must also include the energy of the phonon that the dopant ion will incorporate as it moves with the crystal lattice.

As the temperature of the crystal goes up, the phonon density of states increases (the vibrations of the lattice increase) meaning that more of the dopants will incorporate phonon transitions in their energy level structure. Hence, by definition, there will be less atoms within the zero phonon line, causing an effective broadening of this said spectral line. This discussion will be important when comparing the measurements taken at room temperature to those in cryogenic temperatures. Throughout the thesis the zero-phonon line and the inhomogenous line will be interchanged freely, as they are the same!

2.2 Zeeman splitting

In the presence of a magnetic field the crystal field levels of the dopant ion will split into Zeeman levels. The size of the splitting will be:

$$\Delta E^{(1)} = g\mu_B m_j B_{ext} \tag{2}$$

where g is the Landé g-factor, B_{ext} is the external magnetic field, m_j is the z component of the total angular momentum and μ_B is the Bohr magneton. One can use this Zeeman splitting in order to tailor the energy levels in a coherent manner, leading to more possible quantum computing protocols [19]. The linear relation between the g-factor and the first order perturbation on the energy levels will be important for the last part of this thesis.

2.3 Single instance quantum computing scheme

At the moment, high fidelity single qubit gates have been performed on ensemble qubits. Each ensemble qubit consists of the population of atoms that inhabits a certain frequency channel of the inhomogenous profile. The number of atoms in this type of qubit will be of the order of 10^9! Unfortunately this method scales very poorly namely at a rate of η^{N-1} where N is the number of qubits and η is a small number typically in the range of 0.01 to 0.05, depending on the material in question. This is because the chance that the atoms within a qubit will exhibit a dipole-dipole interaction with the atoms of another arbitrary qubit is typically between 1% and 5%. Even though a low chance still corresponds to a large number of atoms, the probability decreases fast enough for this scheme to not be viable. Furthermore, the long excited state lifetimes of the single ions within the qubit will cause the readout to be slow and of low fidelity. This problem can be solved by using single instances as qubits instead, along with a designated readout ion which has a short excited state lifetime. Using this scheme it is actually relatively easy to find long chains of qubits that all interact with each other via the dipole-dipole interaction [20]. Figure 1(a) and (b) are included as schematics for the explanation of this single instance quantum computing protocol.

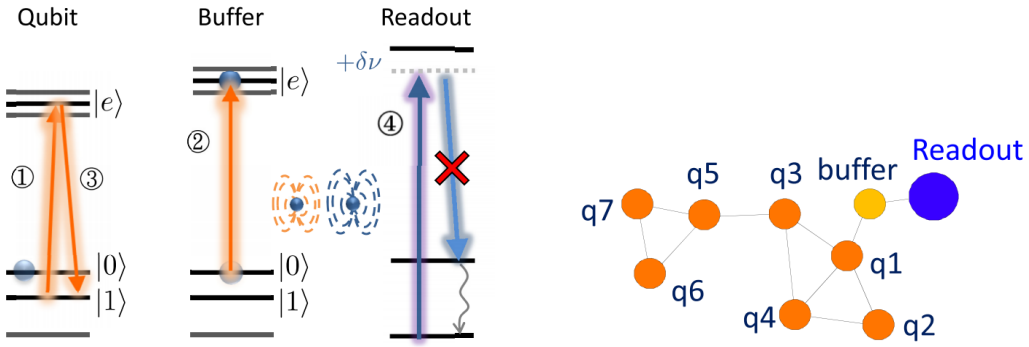

(a) Readout mechanism.

(b) Qubit chain.

Figure 1: The readout scheme and the scalable design of this protocol, taken from [21].

Dipole-dipole interaction and quantum computing

Figure 1(a) shows the underlying idea for how this scheme would work. Say that we have a qubit and it has performed some kind of operation to have now ended up in the $|0\rangle$ state. We then turn a laser on the $|1\rangle - |e\rangle$ transition of the qubit, denoted as (1) in the figure. In this case nothing will happen. Another ion, called the buffer ion, has been prepared so

that it is in the $|0\rangle$ state no matter the state of the qubit. We then start another laser on the $|0\rangle - |e\rangle$ transition of the buffer ion (2). Since the surroundings of the buffer ion have not changed (we were not able to excite the qubit ion) the electron will be transferred to the excited state. Next, in order to not lose coherence in the qubit ion, one performs pulse (3). After this has been done one turns a laser on at the readout wavelength and looks at the fluorescence from the readout ion. Since the buffer ion was excited the surroundings of the readout ion has changed so the laser wavelength (4) will actually do nothing. Hence using this scheme, if the qubit is in state $|0\rangle$ then we will see no fluorescence from the readout ion. For simplicity we call one such chain of events a single buffer transfer (compare this with the ten buffer transfers of Figure 2). The reader can perform the same thought experiment for the qubit in state $|1\rangle$ and notice that the readout ion will fluoresce. Below is a figure of a simulation of the readout of a single europium qubit. Neodymium is used as the readout ion and 10 buffer transfers are performed with a 1% detection efficiency of the setup. The blue corresponds to the qubit being in the $|1\rangle$ state and vice versa for the red. This simulation represents a readout fidelity of 99.7% [21], i.e., the blue and red curve only overlap by 0.3%.

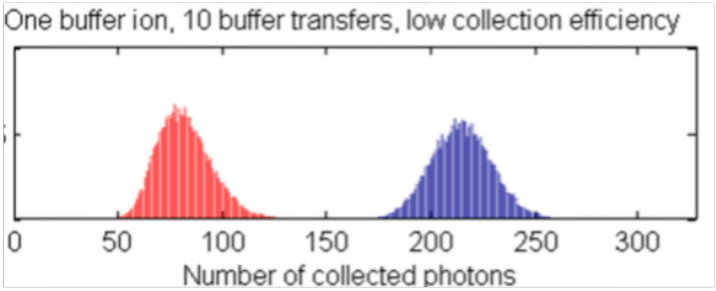

Figure 2: Simulation results for the readout of a single europium qubit using neodymium as the readout ion and the above scheme. This histogram represents a fidelity of 99.7% [21].

Scaling the scheme

Scaling this scheme is in theory straightforward. One starts off by detecting a single readout ion. Once this is completed one starts scanning the frequency of the laser around the buffer ion transition until the readout ion fluorescence has turned off. Once it has turned off, we know that we are at a frequency that targets a buffer ion close enough to the readout ion to be able to interact with it. The laser frequency at which this happens is saved. Then one does the same thing with the first qubit, q1 of Figure 1(b), except that one pauses at each laser frequency and performs the readout scheme until one is able to turn the readout ion on or off. At this point we have a qubit that interacts with the buffer ion which in turn interacts with the readout. At this stage one can just keep doing this until there are no more frequency channels within the inhomogenous line of the qubit ion left that will affect the readout ion!

2.4 The readout ion

The previous section has outlined the scheme for how to efficiently scale the number of qubits in a rare-earth ion doped crystal by using single instances. This scheme however requires a readout ion that has a set of stringent requirements. In fact these requirements would make it a rather bad qubit.

Theoretical requirements for the readout ion

The theoretical requirements for the readout ion are [6]:

1. **Short excited state with a closed transition:**
   In order to increase the fidelity of the readout of the quantum state one wants to be able to detect as many photons as possible during a single readout. This means that the readout atom has to have a short excited state lifetime and a closed two level transition. The last requirement is set because we do not want to end up shelving the electron in another state and reading out less photons than there should be.

2. **No quenching mechanisms:**
   This requirement relates to the previous one in the way that the electron that we are relying on for the readout cannot deexcite to another state, such as a crystal vacancy or another atom.

3. **Large change in permanent dipole moment between the ground and excited state:**
   In order for the scheme to work the readout ion has to have a sufficiently large change in permanent dipole moment between its ground and excited state. This so that the spectral line will shift far enough in one direction when the neighbouring qubit is in a different state. This shift has to be at least larger than the homogenous linewidth of the transition.

4. **Narrow homogenous linewidth:**
   The ideal case is that the homogenous linewidth is lifetime limited. This way, when the line shifts in frequency upon interaction with a qubit, the frequency shift does not have to be too big in order to read the state with high enough fidelity. How narrow we require the homogenous linewidth to be depends on the previous requirement of how far the homogenous line will move due to the dipole interaction. How wide we allow it to be depends on the requirement for a low excited state lifetime.

5. **The readout ion should not interfere with the qubits:**
   The presence of the readout ion should not decrease the coherence of the qubits that are performing the operations. Moreover the readout operation should not induce state changes in neighboring qubit ions.

There are balances to be considered when looking at these requirements. For example one wants a short lifetime, making the homogenous linewidth larger, which in turn will set the requirement for a higher change in permanent dipole moment. This game can be played until the suitable readout ion has been chosen. The final requirement is then to be able to

detect the fluorescence from this single readout ion. This is where, with a lot of help from previous work, this thesis project comes in!

2.5 Cerium as a readout ion

The easier requirement to fulfill when working with rare-earth ion doped crystals is requirement number 5. All the lanthanides will exist, in varying concentration, in any given rare-earth ion doped crystal since they are rather difficult to separate from each other. Consequently, any coherence measurements, or dipole shift measurements of potential qubits already include the contribution from trace amounts of other lanthanides in the crystal. Since we need a closed transition (requirement 1), there is only one ion that naturally has this, namely cerium. The closed transition comes from the fact that cerium only has a single valence electron and no nuclear spin. This transition is the 4f - 5d transition at 370nm, with a lifetime of 40ns (requirement 1) and a lifetime limited homogenous linewidth of full width half maximum (FWHM) 2.9 MHz [22].

When it comes to requirement 3 and 4, [22] reports the change in dipole moment to be 9.6×10^{-30} Cm. This would correspond to a spectral lineshift of 40 MHz ($> \Gamma_h = 2.9$ MHz) at a 10 nm distance from a praseodymium qubit ion. At a distance of 22 nm the line will shift one homogenous linewidth, hence this would be the distance limit. Furthermore the energy transfer between cerium and praseodymium (which would be non-radiative deexcitation going against requirement 2 and interference with the qubit ion, going against requirement 5) is only problematic below 3 nm [23]. This means that a successful readout occurs when the interatomic distance between a cerium readout ion and a praseodymium qubit ion is between 3 and 22 nm. Since the lattice constant of YSO is of the order of 10 Å [24], these distances are easily attainable. In fact [20] shows that using cerium as a readout ion, qubit chains of up to 1000 atoms are easy to achieve with a praseodymium doping concentration of 0.8% and only trace amounts of cerium. The corresponding values for a cerium-europium readout-qubit pair is 2 - 15 nm, making the scalability for these qubit systems approximately the same.

The caviat

Unfortunately, it has been reported on multiple occasions from multiple disciplines that cerium doped in these inorganic crystals has a very long lived trapping mechanism [25]. This could be a showstopper with respect to requirement 2. Paper [26] from this group has reported a hole width of 70 MHz, and an indefinite lifetime. About 50% of the cerium ions get trapped in this state and there is a spatial FWHM of about 5μ m (see Appendix I for the experimental results). Due to the narrow linewidth, there is no other state that the trapping can go through other than the 5d state. Various suggestions have been made and paper [26] includes a simulation that assumes a two photon excitation to the conduction band where the electron is free to move towards its trapping state in the crystal lattice. Nonetheless there is optimism about the possibility of still detecting single ions because of the long time it takes to create this hole and also because a previous paper, [27], has shown that the crystals can be photostable if annealed in a certain way.

A fun-fact about this trapping mechanism in YAG and YSO is that this is the reason as

to why cerium doped into these cannot be used as solid state laser sources. Work is being put into using cerium doped into fluoride based crystal hosts instead for cerium lasing [28]!

2.6 Expected photon count

It is good to do a quick calculation on the number of counts that is to be expected from a single ion. Let us assume that we are at saturation intensity. Then the number of photons radiated by cerium will be on the order of 10^7 s^{-1}. The detection setup has a collection efficiency of 1% leaving us with 10^5 s^{-1}. It was noticed during the thesis that we never really reached saturation intensities so this expected photon count number can easily be lowered by at least one or two orders of magnitude.

2.7 Theory of the detectors

Since we are expecting a low number of counts from a single ion (see section 2.6) it is important to make sure all the detectors are working at their limits. Hence some theory behind them is necessary for understanding how we can get high signal-to-noise ratios (SNR) for the low signal.

Single photon avalanche detector (SPAD)

Detecting single photons without introducing a large dead time between detections along with keeping a low dark count rate is extremely difficult. The trick to any detection of single photons is to introduce some sort of avalanche effect converting a single electron-hole pair, initially created by a single photon, into a detectable current. Photomultiplier tubes, quite common instruments in this field, do this by accelerating the created electron through a series of increasing potentials, where each collision of an electron into a so called dynode (a type of anode plate) creates a large number of copies. After repeating this a number of times, a single electron can be amplified by a factor of up to 10^8. The problem with this is that these need very high voltages (up to 3 kV) and the high currents involved causes there to be a very long dead time in between detections.

An avalanche photodiode (APD) creates an avalanche effect (not quite large enough though) by setting a high reverse bias on a pn-junction so that the electron hole pairs collide with the lattice, ionizing it and thus amplifying themselves. This reverse bias is still too low to fully utilize the avalanche effect as collisions with the lattice damp the amplification significantly. If one is to push this reverse bias past the breakdown voltage of the crystal (working in so called Geiger mode) then an amplification of up to 10^8 is possible, creating the possibility to see single photons, hence the name single photon avalanche detector (SPAD). When at the breakdown voltage, the high currents that are created cause damage to the diode along with long dead times. Most SPADs are thus equipped with electronics that are designed to sink the reverse bias as soon as the breakdown current has been detected, a method called active quenching. More details can be found on Laser Components' Count Blue publication [29].

Charged coupled device (CCD)

Below is a schematic of how a 1D CCD camera works, used for the following explanation:

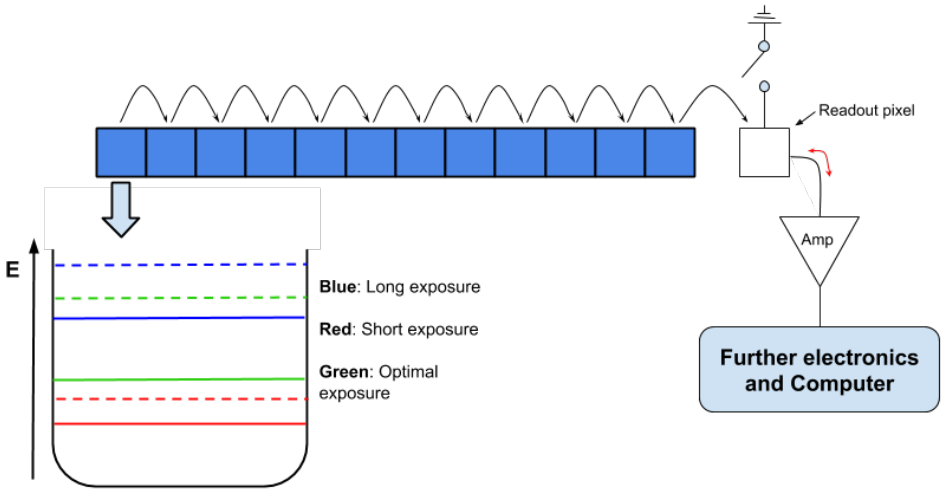

Figure 3: The inner workings of a CCD device. The dashed lines correspond to a signal and the solid lines correspond to thermal noise. The black arrows represent the readout mechanism.

Each pixel consists of a photosensitive MOS capacitor with a corresponding energy well that fills with electrons as photons hit it. If it is uncooled, as the one used in this project, there is a noise floor of electrons created by the temperature of the device, I will refer to these as thermal electrons. If one exposes the pixel for too short a time (the red lines in Figure 3) there will not be a long enough buildup of electrons that are part of the desired signal, causing the signal to noise ratio (SNR) to be low (the dashed red line divided by the red solid line). If one exposes the pixel for too long the heat induced by the incident photons causes the noise floor of thermal electrons to increase (the blue solid line in Figure 3). The signal will also increase, (blue dashed line) however the SNR will not be much better than for the red case. Furthermore now that we have nearly filled the well, electrons will tunnel/overflow into adjacent pixels, causing the image to be smudged, termed bleeding in the field. There exists an optimal exposure time (that depends on the signal strength), which gives a lowest possible SNR, shown in Figure 3 as the green line. Here the pixel has not become too warm and the well is not overflowing. For the spectrometer used in this project along with the low signals, this optimal exposure time is 0.06 s (see Appendix D for more details). For more information on the inner workings of a CCD camera see chapter 8.2 of [30].

There is another mechanism that can introduce noise in the CCD signal that is well documented in chapter 3.9 [31]. The readout of the pixels works in a train like fashion, where the potential barrier between each pixel is modified such that the electrons move one step to the right for each pixel readout (shown as the black arrows). The readout pixel is then connected to an amplifier that will output the number of counts within the given well. The amplifier and readout pixel are in a thermal equilibrium (marked as the red two sided arrow) meaning that at high gain, the amplifier will supply the readout pixel with extra

noisy electrons in a very sporadic manner. This noise source can be quenched by grounding the readout pixel for a longer amount of time between each pixel readout when at high gain operation. This grounding time was set as 0.06 s as well although it could have been investigated more thoroughly.

2.8 Past results

A lot of work has been put into developing a working system and trying to detect single cerium ions, however this result has evaded the group. The main hint to this not working comes from the the measured zero phonon lines. These have been eerily continuous, when at such low concentrations and at high enough detunings, they should exhibit a discrete structure (the statistical fluctuation in the number of atoms at a given point of the inhomogenous line goes as $\sqrt{N}$). The point at which single ion detection was left off was at the following figure, where a raster scan $12.5\mu\text{m}^2$ in size was performed trying to find a clear fluorescence spot in some part of the crystal. As is visible there is nothing conclusive.

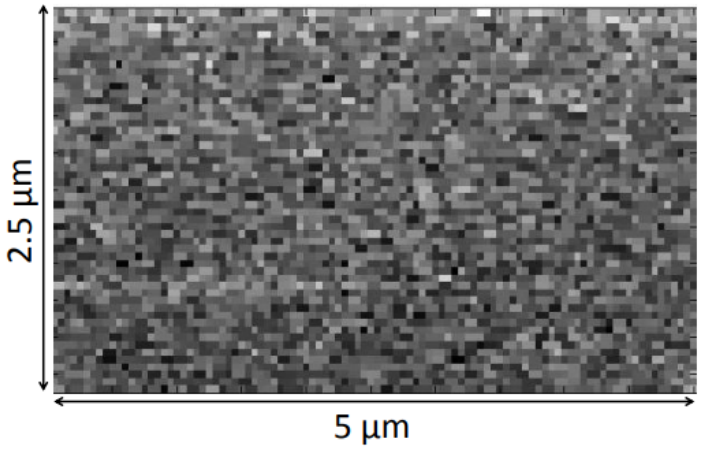

Figure 4: A raster scan over a $12.5\mu\text{m}^2$ area at $\lambda_{ex} = 370.799$ nm. One could argue that there could be signals from a single ion, however there is nothing conclusive.

The main hypothesis for the reason as to why single ions have evaded the system, is that cerium ions from outside the focus contribute to a noise floor that is higher than the signal from a single ion. This will be further discussed in section 4.

3 Equipment

Detecting then manipulating single ions sets demanding requirements on the setup used for the purpose. The following section addresses these requirements, describes how they are attained then discusses some details that were noticed and maybe fixed during the thesis work.

3.1 The requirements on the setup

In order for the single ion readout scheme to work, the setup needs to be spatially and spectrally stable enough to manipulate a single ion for a longer period of time (while the other qubits perform an algorithm). This entails that one: the setup should not spatially drift more than about half a micron (set by the laser focal size); and two: the laser frequency should not drift past the homogenous linewidth of the readout ion, of the order of 3 MHz in this case. The frequency stability is not as high as one would expect, since the readout scheme only uses a binary on or off signal in order to work. Therefore as long as one is close enough to the center of the ion's homogenous line such that this binary signal is resolvable the readout scheme will work, albeit with varying fidelity. In terms of Figure 2, a non-resolvable signal would be when the two histograms overlap. The frequency stability is solved using a Pound-Drever-Hall (PDH) laser stabilization setup and the spatial stability is solved by using a home made microscope holder.

Another aspect to be considered is the fact that there are billions of atoms in a crystal so tight spatial resolution is required. This is solved by using a homemade confocal microscopy setup, where the details are included in [32].

PDH stabilized diode laser for frequency stability

The laser used is a 370 nm diode laser with a homemade external Littrow cavity built on. The angle of the grating in the Littrow cavity is controlled by micrometer screws for coarse adjustment and piezoelectric transducers for fine adjustments in laser power and wavelength. This passive system alone limits the laser linewidth to the order of 1 MHz [33]. However, it will drift far past the 3 MHz requirement that we have set, hence some active stabilization method is required.

Active laser stabilization methods are always based on measuring the phase or frequency of the laser beam, compare it with some stable reference then adjust the optical length of the laser cavity in one way or another. If one is to use the transmission of laser light through a reference cavity, the optical buildup time will not allow for any fast stabilization signals. Furthermore one cannot distinguish between the intensity fluctuations of the laser from frequency fluctuations. Wavelength modulation techniques that look at the transmission through an optical reference cavity while modulating the laser frequency suffer from the same problem. This distinguishability can be attained by looking at the reflection of the signal from the reference cavity instead. Moreover, the reflection signal is instant so fast stabilization is possible. Along with some modulation of the wavelength one can then know which side of the resonance line of the cavity the laser is on. Pound-Drever-Hall (PDH) stabilization does just that! There is a lot of literature about this technique where the

review paper by Eric D Black [34] is a good read. For an even more intuitive and detailed account I refer to chapter seven in the PhD thesis of Lars Rippe [35].

The PDH locking system of this laser setup attains a linewidth of 300 kHz while locked. From the homogenous linewidth of cerium, a 300 kHz linewidth corresponds to a 4% fluctuation in the fluorescence intensity. All the details of the setup are included in [33] and the latest measurements of all the parameters in the setup are included in Appendix B and C.

Confocal microscope for spatial and depth resolution

As has been mentioned, a tight spatial and depth resolution is absolutely necessary in order to have a chance to detect a single ion. The method of choice in order to attain this is confocal microscopy. The spatial resolution of a confocal microscope differs from wide field microscopy since it includes double spatial selection, namely from the excitation volume (the laser beam is tightly focused) and the collection volume (there is a small pinhole in the collection path). In other words the probability of detecting an emitter in a given volume, is the product of the excitation probability of the emitter and the collection probability of a photon from that position. Given that the image of the pinhole on the excitation focus is Gaussian and the excitation volume in itself is Gaussian, the theoretical spatial resolution of a confocal setup, $\omega_{confocal}$, in the radial direction is set by the waist of the product,

$$w_{confocal} = \frac{1}{\sqrt{\frac{1}{w_{laser}^2} + \frac{1}{w_{pinhole}^2}}}. \tag{3}$$

The w's of Equation 3 correspond to the waists of the laser and the pinhole assuming $\omega_{pinhole}$ is imaged on ω_{laser}. In total a 300 nm spatial resolution has been reported for this setup [32].

Using the same discussion as above, except that the intensity of the excitation laser and image of the pinhole is Lorentzian along the depth axis, one can show that a confocal geometry also provides acute depth resolution. The intensity from different positions in the depth direction will fall as z^{-4}, to a first approximation.

There are further, more subtle advantages of using confocal fluorescence microscopy for single cerium ion detection. The first aspect is that the resolution is set by the excitation wavelength, which, in our case, is shorter than the fluorescence. Since the diffraction limit of shorter wavelength light is smaller, the resolution will be higher. This differs from a conventional microscope where the resolution is dependent on the longer wavelength fluorescence. On the downside, this difference between fluorescence and excitation wavelength can decrease the depth resolution since there is an uncertainty in position of the order of λ. If one defines $\beta = \lambda_2/\lambda_1$ where λ_1 is the fluorescence wavelength and λ_2 is the excitation wavelength, then the depth resolution decreases as β increases. The following figure illustrates this fact, along with the fact that one really wants to work as close to $\beta = 1$ as possible. Furthermore the curves of Figure 5 never actually go to zero, meaning that the incoherent fluorescence light from behind the focus is never fully sectioned away.

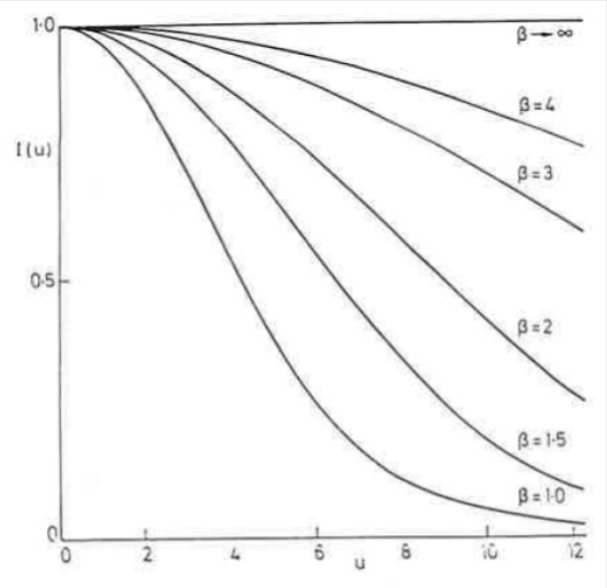

Figure 5: The transmission of an incoherent light source at a distance u away from the focus of the imaging lens, where β is defined as the ratio between the fluorescence wavelength and the excitation wavelength (λ_2/λ_1). Figure taken from page 45 of [36].

It must be noted that the x-axis, denoted as u, is in the dimension of some normalized length unit that is the same for any confocal system:

$$u = \frac{8\pi}{\lambda} z \sin^2(\alpha/2), \tag{4}$$

where NA $= \sin\alpha$ and λ is the excitation wavelength. Note that this is only true for an object radiating incoherent light. The depth sectioning ability of confocal imaging is slightly different for coherent light sources. This will however not be included here.

In the case of cerium, β is always between 1 and 1.4, however, using one of the available bandpass filters for all single ion detection would bring β down to 1.15, improving the optical sectioning in the depth axis.

The sample and microscope holder

In order to be able to profit from a confocal geometry, a very tightly focusing lens has to be used. The lens used is a BluRay lens that has a focal length of 1.2 mm and a diameter of 3 mm. With a numerical aperture of 0.85 if can focus a 3 mm laser beam of wavelength 370 nm to a focal size of about 1μm. However, because of this tight focus it has to be placed very close to the sample, hence it has to be mounted in a way so that it can fit into the sample space of the cryostat.

The following figure is a picture of the microscope holder before we made minor adjustments to it. Since confocal microscopy only images points, one needs three dimensional positioning possibilities. Therefore attocube nanopositioners are mounted onto the holder (see section 3.2 for more details about these).

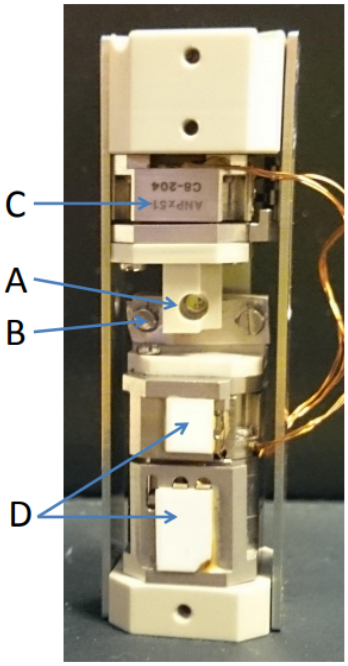

Figure 6: The microscope holder before adjustments. A is the lens holder with the BluRay lens mounted in it, B is the sample holder and C and D are the attocubes used to scan the sample in all three dimensions.

3.2 Attocubes

The attocubes are nanopositioners that make use of piezoelectric transducer crystals along with a 'slip and stick' mechanism. For the explanation I have added attocube's own schematic in Figure 7 with their permission. A slow voltage ramp is applied to a piezo crystal, moving a rod (m_2) upon which a stage (m_1) rests. This corresponds to the step from A to B in Figure 7. When the crystal has reached its maximum size the voltage is quickly dropped so that the rod comes back to its original position but the stage has not moved (B to C). This is exactly equivalent to when one pulls a tablecloth really quickly from under porcelain. Due to the impulse, the porcelain stays on the table while the tablecloth slips away from underneath it.

As can be seen in the figure, the corresponding electric signal that does this is a sawtooth. Therefore by varying the frequency and the maximum voltage of the input sawtooth, it is possible to control these attocubes very precisely. Since this is a process that depends on friction, these parameters must be calibrated for each attocube in order to attain optimum functionality. This 'slip-stick mechanism' allows the attocube to benefit from the micrometer positioning precision that piezos offer along with a long scanning range!

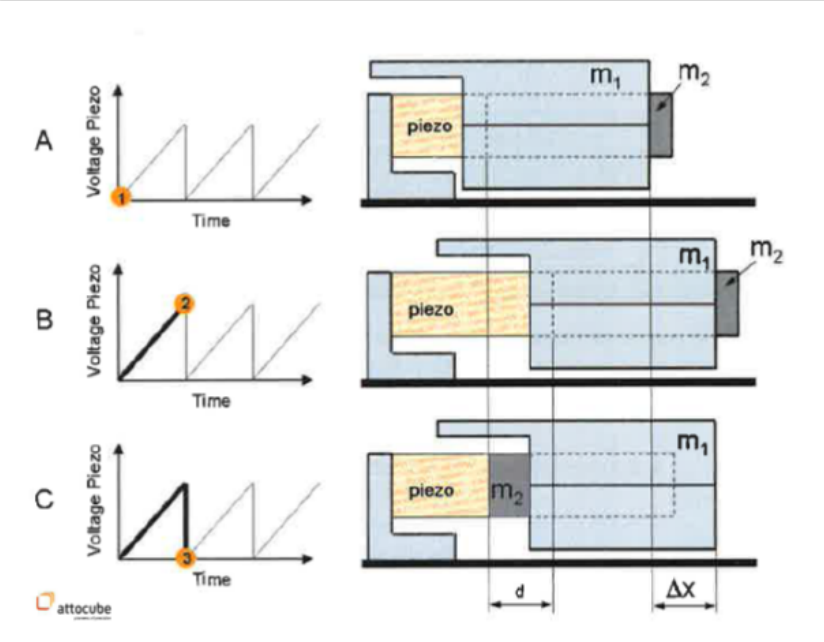

Figure 7: A schematic of the slip and stick mechanism in the attocubes. Printed with the permission of Attocube Systems AG.

An extra feature that is added to the attocubes used in this thesis is a resistive readout sensor. This means that we can readout where the stage m_1 is positioned in micrometers, to an accuracy of (by specification) 200 nm.

However, due to their size they only exert a force of about 1 N on the moving stage so any misbalance introduced during the mounting process or anything small in the way (such as water droplets) may hinder the positioners from working properly. Furthermore the readout sensor and its corresponding cabling out of the cryostat showed itself to be extremely sensitive and most of the time did not even work properly. This was quite a problem that was not solved during the thesis work. For more details of these and possible solutions problems see Appendix E.

Throughout this thesis, a LabView program that uses the position feedback from the resistive sensors and moves to the desired position with a certain failure limit was used, essentially forcing the attocubes into doing what we wanted them to do. This method worked for finding single microcrystals however will not be adequate for single ion detection.

3.3 Full setup

The following figure is a schematic of the full setup, including an imaging system whose purpose is to obtain a reflection image of the sample. The blue lines correspond to the excitation light at 370 nm while the purple lines correspond to the fluorescence! The lenses l_p are the lenses in front of and behind the pinhole and have a focal length of 50 mm while the lenses l_i are the lenses used for the imaging system with a focal length of 100 mm.

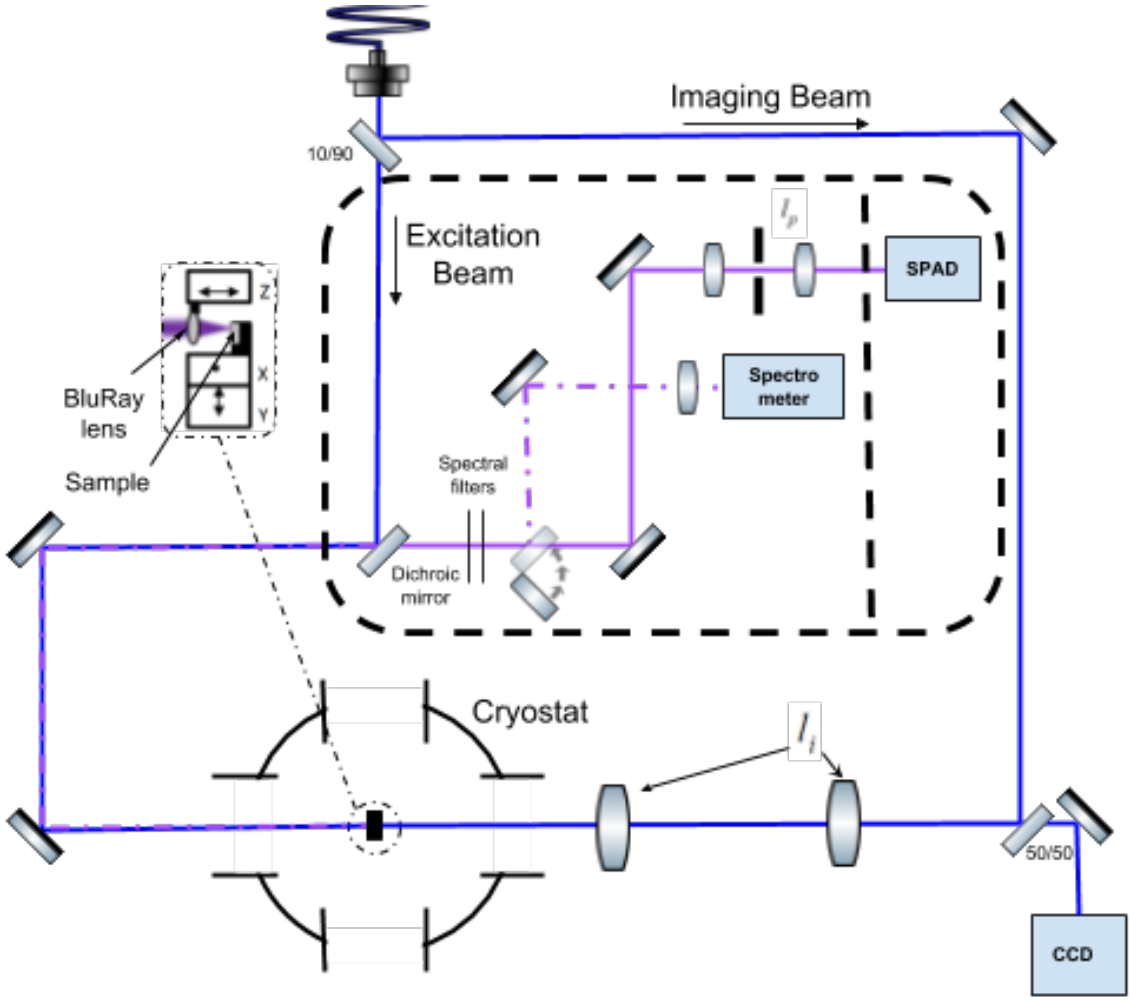

Figure 8: A schematic of the full setup used throughout this thesis work including the holder with the attocubes, BluRay lens and sample.

The holder is included as a zoom in on the bottom left of the schematic. The z-direction is defined as moving the lens closer and further away from the sample, the y-direction moves the sample up and down and the x-direction moves the sample right and left. For more exact details of the setup and detection part, see Appendix D.

4 Simulation

The following section outlines the thought process and the creation of a simulation who's purpose it is to understand why single cerium ions have not yet been detected in bulk. It has been assumed that the background signal from ions behind and in front of the focus have contributed to a noise floor that is higher than the number of counts from a single ion. Hence a simulation that ray traces fluorescence from various positions inside a crystal, through the optical detection system and a pinhole was created.

It is divided into two parts, the imaging system, simulated using ABCD matrices, and the crystal, where fluorescing centers are placed inside a crystal at random and are made to fluoresce with an intensity dependent on the intensity of the excitation laser at their given positions.

Before continuing it is important to note that this simulation works within the geometrical approximation, i.e., the angles are low and the apertures through which the light passes are much larger than the wavelength of the light. This is not quite true for the setup in use, since the BluRay lens has a numerical aperture of 0.85, focusing the light down to its diffraction limit. To a first approximation this simulation will however do a good job, as is described in [36] but more discussion around this will be included in later sections.

4.1 Imaging with a ray-tracing simulation

Following is a schematic and table of the variables that will be of relevance to the simulation. This should be used in conjunction with further reading of the section since the variables have no meaning quite yet. It is depicted for one dimension, however, due to the rotational symmetry of the system, these values are easily converted to areas by squaring.

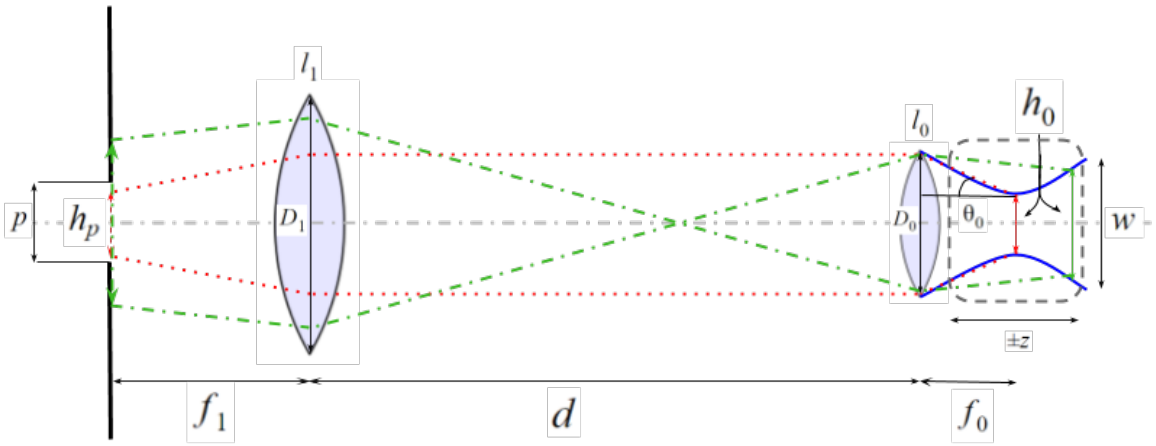

Figure 9: A schematic of the included variables in the simulation. The optical system and the crystal (the grey dashed box) with randomly placed cerium ions is shown. Table 1 indicates what the individual labels mean.

Table 1: The labels and their corresponding values from Figure 9.

Label	**Value in simulation**	**Comment**
l_0	NaN	The BluRay lens
l_1	NaN	The lens before the pinhole
f_0	1.2mm	The focal length of l_0
f_1	50mm	The focal length of l_1
D_0	3mm	The diameter of l_0
D_1	2.54cm	The diameter of l_1
h_0	w	The size of the object (set as the waist size of the excitation beam)
h_p	Simulated result	The size of the image of h_0
p	25μm	The diameter of the pinhole aperture
d	2m	The distance between the two lenses
z	$[-100, 100]\mu$m	The distance from the focus, f_0

The aim for simulating this imaging system is to place an object on the rightmost end of the schematic in Figure 9 (shown as a solidly drawn arrow in red or green) then projecting its image h_p onto the aperture p, at the leftmost part of the schematic (shown as the dashed arrows at the aperture opening). By varying the position of the object with respect to the focus of lens l_0, the simulation gives a value for how much of the image, h_p, goes through the aperture p. Consequently, varying z will give an impulse reaction function (IRF) of the optical setup for the depth dimension. The following equation summarizes this:

$$\mathrm{IRF}(z) = \left(\frac{h_p\big(h_0(z)\big)}{p}\right)^2 \left(\frac{R_1\big(h_0(z)\big)}{D_1}\right)^2. \tag{5}$$

The reader sees that there are two parts to Equation 5. The first bracket represents the fraction of the final image area that goes through the aperture. This part is done by raytracing the image with size h_0 at position $f_0 + z$ through the optical system using ABCD matrices for each optical component (see Appendix J). The second bracket illustrates the fact that l_1 is not infinitely large, so only a certain amount of light that has a high angle after l_0 will even hit l_1. This is easily included by looking at the size of the ray bunch of h_0 at l_1, named R_1, and only include the percentage of this ray bunch that hits the lens. Squaring will again give the area ratio. From the way Equation 5 is written the reader can see that the two fractions depend on the size of the *object*, which in turn depends on its position with respect to the focal position of the lens (f_0). This is forced upon the simulation to include the fact that the object to be imaged is in fact fluorescence from ions within the excitation volume. Hence h_0 is equivalent to the waist of a Gaussian laser beam focused by lens l_0 (see Equation 6 for this calculation).

Finally looping around the variable z will give an impulse reaction function for the optical setup, shown in the following figure:

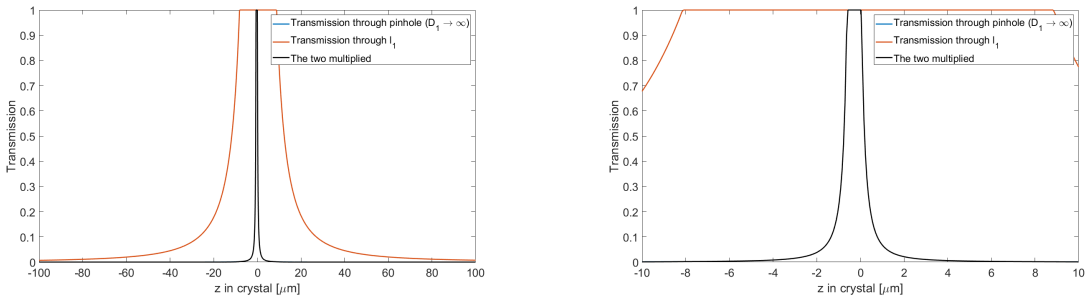

(a) Transmission of the pinhole setup

(b) Zoom in

Figure 10: The impulse reaction function of the optical system as described above. These values correspond very well with the already published values in [37].

This impulse reaction function is slightly larger than the one calculated on page 61 of [37], most probably due to the fact that the object increases in size outside of the focus, a parameter that was not included there. It is important to note that since this was done in ray optics, the individual brackets of Equation 5 go to very high values when imaging an object at the focus. This since the image h_p and the ray bunch size R_1 will be much smaller than the apertures through which they pass. This was amended by setting the condition that if the whole image goes through the aperture, then the IRF is set to one, seen in Figures 10 (a) and (b) as the plateau around $z = 0$.

It might seem intuitive that the IRF is a symmetric function around f_0, however, this is not quite true. This since the angle subtended by l_0, θ_0, is larger at $-z$ values (corresponding to an object closer to the lens than the focus). Even though this means that more light will enter the detection setup, the angle with which it enters will be higher giving the lenses l_0 and l_1 a harder time focusing the image down to the aperture. This fact will be used and discussed in the results section.

4.2 Fluorescent centers in a crystal

Now that we have an IRF, the object, h_0, needs to be created. The aim behind this part of the simulation is to add fluorescent centers (in our case cerium ions) into the beam path at varying z, then bin their collective intensities as a function of z. Each 'z-slice' will then be multiplied by the IRF to obtain a value attributed to how much of the intensity from that given slice enters the detector.

Density of cerium

The random emplacement of ions' positions is controlled by some density function, ρ, that is uniform with respect to position but dependent on the population's inhomogenous linewidth, homogenous linewidth and doping concentration. Given that the excitation laser has a linewidth of 300 kHz ($<< \Gamma_h$), the density of cerium ions as a function of detuning from the center of the inhomogenous line has already been calculated by [37]. In this calculation it is also assumed that the crystal has a doping concentration of 10^{-7} (the same used throughout

the experimental work of this thesis) and the laser power is assumed to be at cerium's saturation intensity, meaning that the homogenous line is broadened to ≈ 5.7 MHz.

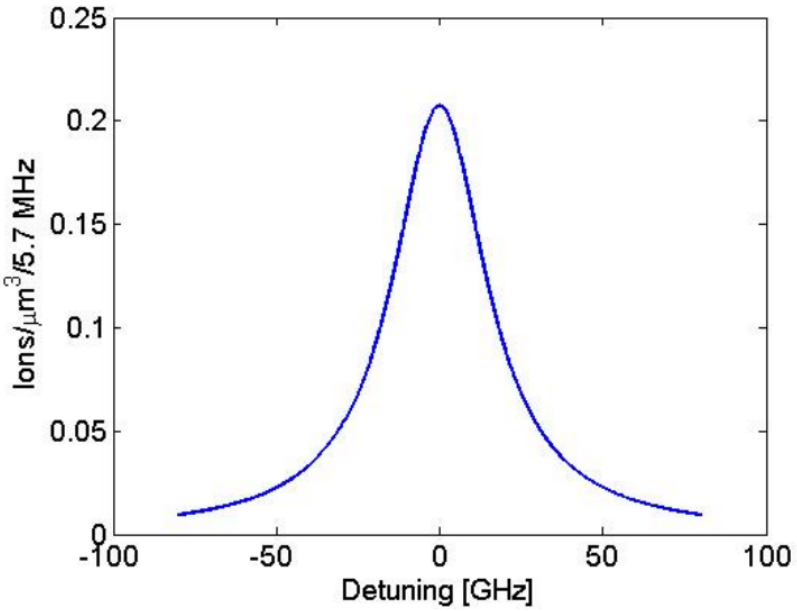

Figure 11: The number of ions per cubic micrometer as a function of detuning from the line center. This plot assumes a homogenous linewidth of 5.7MHz and a cerium concentration of 2000 ions/μm^3 (corresponding to a doping concentration of 10^{-7}). The peak value is 0.21 ions/μm^3/5.7 MHz.

The values of Figure 11 will be used as my input variable in the simulation to control the concentration of ions within the excitation beam volume.

Fluorescence

The intensity at which the cerium fluoresces is controlled by the intensity with which they are illuminated. Since the excitation light is a fixed quantity, the illumination intensity will boil down to only depend on the ions' position. The problem is rotationally symmetric around the axis of propagation, z, thus all we need to know is the radial intensity of the beam with respect to the position in z. This is dictated by Gaussian optics where the waist $w(z')$ of the beam, i.e., the radial distance between the points where the beam has lost $1/e^2$ of its intensity, is given by:

$$w(z') = w_0\sqrt{1 + \left(\frac{z'}{z_0}\right)^2}. \tag{6}$$

Here w_0 is the beam waist at the focus, calculated to be 1μm, z_0 is the Rayleigh length of the beam, calculated to be approximately 10μm and z' is the position after the lens given by $f_0 + z$ (w.r.t Figure 9).

The following equation gives the light intensity at a given radial position with respect to the beam's waist size at that same position:

$$I(r, z') = \frac{2P}{\pi w^2(z')} \exp\left[- \frac{2r^2}{w^2(z')} \right], \tag{7}$$

where r is the radial position, z' is, in our case, the distance from the BluRay lens, $f_0 + z$, and P is the power of beam. A sanity check is that Equation 7 gives the saturation intensity at the focus for an input power of 15μW, exactly like in the literature [26].

The intensity at which the ions will fluoresce will then be linear with the intensity of the excitation light until one comes close to saturation where the population in the upper state will not be able to exceed 1/2 of the total population. In fact up to I_{sat} the fluorescence intensity will be:

$$N_{photons} = N_{sat} - \frac{N_{sat}}{1 + \frac{I}{I_{sat}}}, \tag{8}$$

where I_{sat} is set as the experimental value of 1.4 W/m^2 and N_{sat} is the number of photons that should be emitted given that we are exciting Cerium at saturation intensity. This value is set to 75×10^3 (page 85 [37]). In the simulations below it will be seen that the saturation fluorescence will in fact be 3.75×10^4. This was simply a mistake, however, the principle remains the same.

Final figure

The following figure is an image of a crystal with a cerium concentration that corresponds to the center of the inhomogenous line ($\rho = 0.21$ ions/μm^3 from Figure 11) along with the corresponding fluorescence intensity due to the power of the laser beam entering the crystal. The fluorescence intensity of each ion is shown as a color (see colorbar) in a log scale for the purpose of illustration.

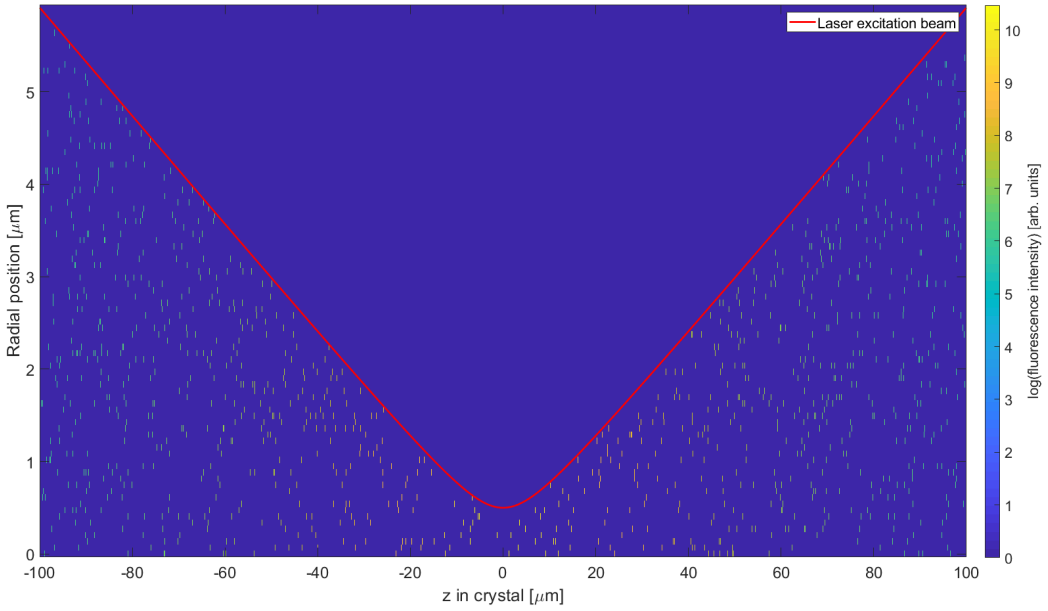

Figure 12: The logarithm of the fluorescence intensity of Cerium ions (see colorbar) as a function of their position with respect to the focus of the laser excitation beam. One can see that the fluorescence intensity drops as one goes out to the wings of the excitation beam, as is expected!

Figure 12 is created by placing ions in a cylinder corresponding to the size of the laser beam and then realizing that their fluorescence intensity will only depend on their radial position (as has already been discussed). Hence the volume can be boiled down to the image of Figure 12 which illustrates how the ions at the focus will fluoresce at an intensity corresponding to their saturation intensities (depicted in yellow) while ions at $z = \pm 100\mu$m will fluoresce at much lower intensities (more blue in tone).

Creating an object to image

Once one has cerium fluorescing from a crystal as in Figure 12, it is necessary to bin these intensities as a function of z (the distance from the focal point). This will be used as the image h_0 that goes through the optical setup. The binned intensities of each layer in z will give the following histogram where (a) is for the whole 200μm thick crystal and (b) gives a zoomed in version of it.

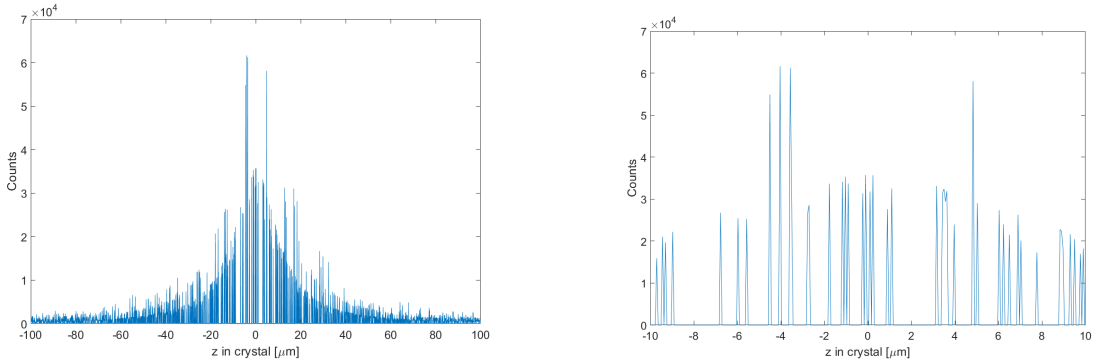

(a) Full crystal length.

(b) Zoomed in.

Figure 13: A histogram of the summed intensity of each 'z-slice' in the crystal. 3.75×10^4 counts corresponds to an ion fluorescing at saturation, as is the case around $z = 0$.

We see from (a) that even though there is no optical detection discrimination and there are more atoms within the excitation beam as one moves to larger z, there will still be a steep decrease in intensity away from the focus. This is due to the fact that the excitation intensity drops as a fast Lorentzian along z, owing to the tight focus of the BluRay lens. Another aspect that is clearly visible in (b), is that the atoms that are just in front of and behind the focus will actually contribute the most to the signal. This since the intensity of the excitation beam here is still rather high, along with the fact that there are more atoms in these slices (on the order of 2 - 3 as compared to about 1 in the focus).

4.3 The Final Product

Finally Figure 13 (a) should be multiplied by the IRF of the detection system, Figure 10 (a), in order to find out what the detector will see.

It can be seen that the result of this, Figure 14, is that in the focus there is a layer with a single atom that will fluoresce at saturation intensity and the atoms from other layers will be suppressed by the IRF. However, a SPAD integrates over all signals, meaning that there is no way to discriminate between them. In fact the signal to background ratio (SBR), where the signal is the highest peak of Figure 14 and the background is taken to be the sum of all other peaks, in this case is 0.3. Hence for this simulation it will be impossible to detect a single ion since the fluorescence from layers outside the focus will contribute to a noise floor that is approximately three times higher than the single ion fluorescence level.

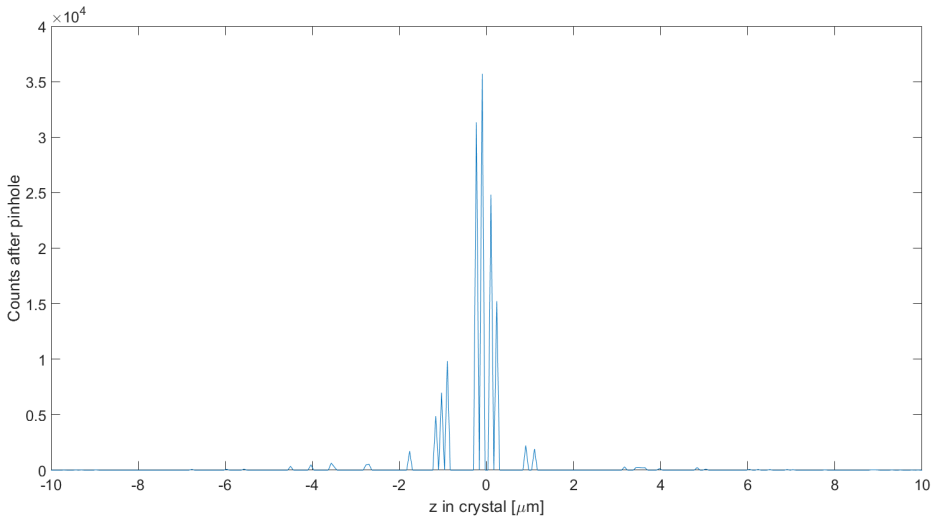

Figure 14: A figure of the final result of the simulation, where fluorescence from randomly placed atoms is projected onto the pinhole. This is the product of Figure 10(b) multiplied by Figure 13(b).

4.4 Simulation results

It is interesting to look into what the SBR is as a function of cerium concentration in the crystal to be able so see when a single ion can possibly be detected. Due to the random nature of the simulation, it was run 200 times for a given concentration before the SBR was extracted and plotted. Figure 15 shows the results of those simulations, where the black line indicates an SBR of 1.

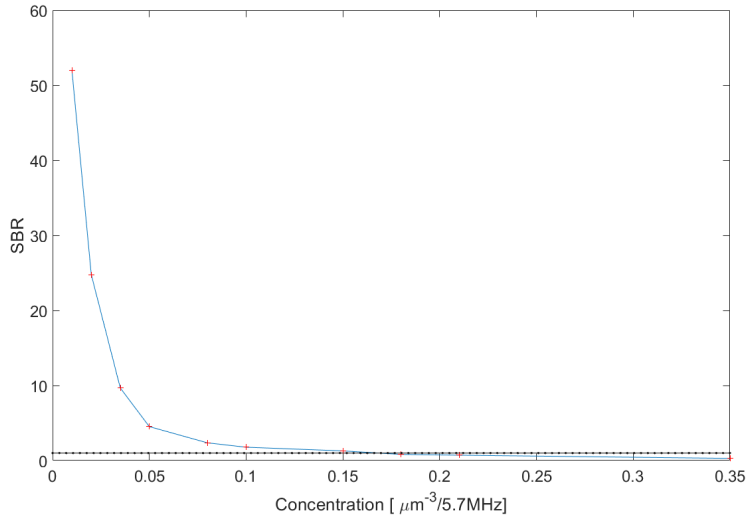

Figure 15: The SBR of a single cerium ion as a function of crystal concentration. The black line corresponds to an SBR of 1. Any points above this are occasions when it is possible to detect single cerium ions.

As the reader can see, only at concentrations of 0.1 ions/μm^3, corresponding to a detuning of $\approx$ 20GHz (extrapolated from Figure 11) can a single ion be seen. At even higher detunings (lower concentrations) single ions should be detectable.

Geometrical optics approximation

As has been mentioned previously this simulation works within the framework of geometrical optics. The place where this approximation fails, is that it will focus the rays to an infinitesimal point at the focii of the lenses, when we know that, due to interference effects of the light with itself, this is impossible. With respect to the IRF, the geometrical approximation would predict that with a small pinhole, its FWHM will keep decreasing all the way to zero. In fact this is not quite true, since at small aperture sizes, even the light from the focus will not be able to be focused down through the aperture, so the optical sectioning will be just as bad as for a larger pinhole. This failure of the geometrical approximation is partly solved by setting the transmission to one when the whole image goes through the pinhole (as has been mentioned previously). All in all however, the geometrical approximation does an OK job to the first approximation.

Possible reasons as to why single cerium has not been detected

Given the results of the simulation presented in Figure 15, there are a few possible reasons that could explain why single cerium has not yet been detected:

1. **Setup deficiencies:**
   A thorough discussion about abberations in the optical system has already been brought up in [37] and it was concluded that these effects were negligible during the characterization of the setup [32]. However, as described on page 99 of [36] when applying confocal imaging systems experimentally, depth discrimination is very sensitive to the presence of any pupil function aberration or deficiency. It suffices that some optical component is slightly misaligned for the simulated IRF to be experimentally incorrect. A hint to this comes from a depth sectioning measurement of the setup performed by Jenny Karlsson (see figure 6.21 on page 75 of [37]). It turns out that in this measurement the confocal sectioning ability is highly compromised, possibly letting more light through from the layers outside the focus!

2. **Other background sources:**
   No other background sources have been taken into account in these simulations. It is enough that something else in the system fluoresces at a higher intensity than a single ion for it to be undetectable. There is a large possibility that this is the case as will be seen in the coming sections.

3. **Discrimination between individual ions:**
   It could be that when one moves around in the sample, the signal from a single ion does not decrease enough before one starts collecting the signal from another ion. This could be implemented and checked with the simulation by simply moving the IRF along z and tracing the signal from the various peaks. Due to time constraints this was not implemented.

4. **Conclusions from [37] and [38]:**
   There is a plethora of conclusions from Jenny Karlsson's, and Ying Yan's work with single ion detection. To include one, the fact that they had never seen any discrete structure in the inhomogenous profile, could mean that the dopant concentration is wrong, or the confocal volume is actually quite different to what we think it is. If interested the reader can refer to pages $83 - 88$ in [37].

5 Experimental Results

This section will present all the experimental work that was done during this thesis work.

5.1 The new idea!

Even though simulations say that there is a possibility of detecting single ions in bulk, it was decided to work with microcrystals nonetheless. The main reason is the fact that in microcrystals there will only be a few cerium ions within the excitation beam in the depth direction since we have essentially cut away all other cerium from behind and in front of the focus. This will greatly increase the chance of seeing something. Furthermore if no single ions are seen, maybe we can get some more answers!

Microcrystal simulation

The following figures show randomly placed cerium ions (depicted as filled circles) within the laser excitation beam and a crystal depth of 20μm. These figures have been simulated in the same way as in section 4 for different two different detunings.

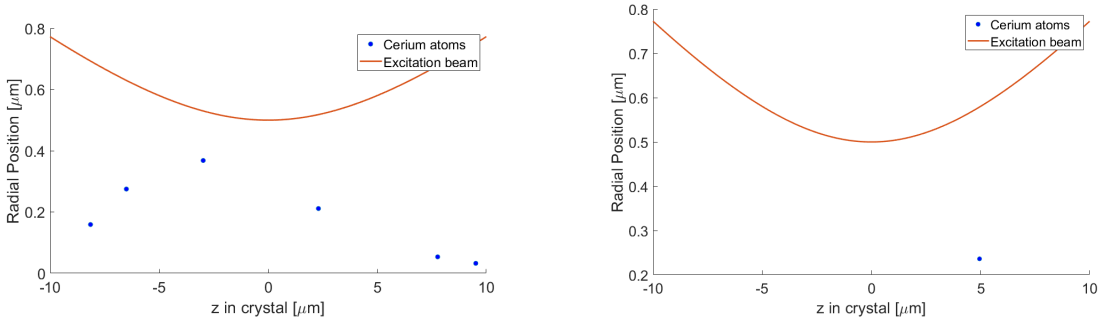

(a) 0GHz detuning

(b) 30GHz detuning

Figure 16: Randomly placed cerium ions within the laser excitation beam at a concentration given by the detuning. As can be seen there is actually only a single ion within the beam at a relatively small detuning of 30 GHz and a crystal depth of 20μm.

As can be seen from the figures it is possible that there will only be a single atom within the excitation volume, given the correct detuning and crystal thickness. However, the number of cerium ions for a given detuning will go up as $(\text{size})^3$, so small crystals are essential! The easiest way to achieve these small sizes is to crush a bulk crystal into microcrystals, as shown

in Figure 17. Sifting the final product through various strainers, divided the crystals into three different size dependent categories, namely: $70 - 100\mu$m, $40 - 70\mu$m and $10 - 40\mu$m. The $40 - 70\mu$m samples were used throughout this whole result section.

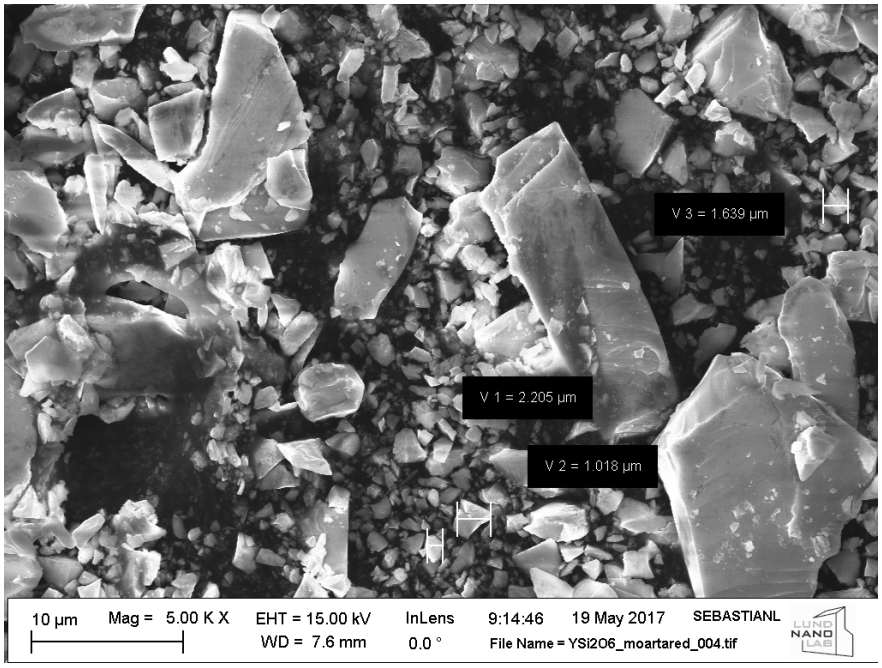

Figure 17: A scanning electron microscope (SEM) picture of the crushed bulk crystal taken at NANO-Lund. As one can see there are various sizes in this picture ranging from 1 to 30μm. They were then sorted by sifting them through a strainer.

Another quite nice aspect about this size of microcrystals is that they are just right to be a mixture between not many ions within the excitation volume, and, theoretically surface effects not playing a role, since these effects occur before about 5μm depth.

5.2 Suitable mounting of the microcrystals

The microcrystals need to be mounted in a way such that they can cope with cryogenic temperatures and the materials used for the mounting should not optically interfere with the cerium signal.

Substrate

After some discussion with Ivan Scheblykin the initial idea was to use some substrate and then place the microcrystals on this substrate using a polymer. Three different substrates were tested for their fluorescence properties, namely black silicon, quartz and glass. Neither quartz or black silicon fluoresced in room temperature. However, if the focus was tight enough the glass would fluoresce locally in yellow. It is a known fact that microscope slides are doped with various dopants in order to strengthen their crystal structure. Furthermore the glass crystal has many defects which produce vacancies and color centres. Therefore it is sensible

to attribute the fluorescence to two photon excitation processes in these colour centres. As a sidenote these color centres went from yellow to green during the cooling process from room temperature to 2 K. The explanation to this comes from the same explanation that LEDs change color as they are cooled, namely that the lack of phonons causes the average lattice constant to be smaller, hence the bandgap larger! Black silicon was completely black at all temperatures and positions, however, it was not chosen as the substrate since it does not transmit any light whatsoever and we wanted the flexibility of coming in with our excitation beam from any direction. Finally quartz was chosen as the substrate since it did not exhibit the same problems as glass and is transparent to UV. However, we were not quite sure what sort of quartz we have, and when it fluoresced in green at some positions, like glass, it was decided that this should be something to work on for the next round of measurements. Below is a figure showing the transmission of various kinds of quartzes. As can be seen, as long as they are pure most will transmit far into the UV!

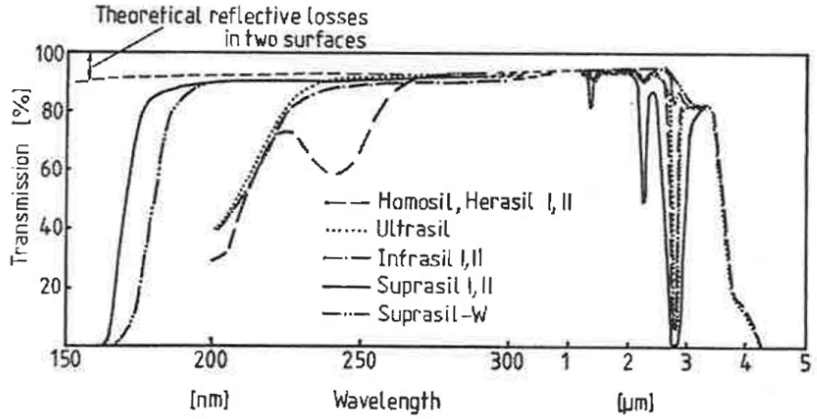

Figure 18: The transmission curves for various qualities of quartz. The top dashed line, marked as the theoretical reflective loss draws the curve of reflective loss using only the Fresnel equations. This exhibits an upper bound to the transmission. Figure taken from page 143 of [39].

Mounting polymer

The initial idea was to use Poly Methyl Methacrylate (PMMA) as the polymer adhesive between the microcrystals and quartz. After this was tested in cryogenic temperatures it was not quite sure what was creating a fluorescing background in the signals. After looking into the absorption profile of PMMA, see the top panel of Figure 19, it was decided that one should change this to Polydimethylsiloxane (PDMS) since its absorption edge is far below 370 nm (line (H) in Figure 19). Furthermore there is a higher chance of refractive index matching since the absorption profiles of some of the quartzes and PDMS look quite alike (compare Figure 18 with Figure 19).

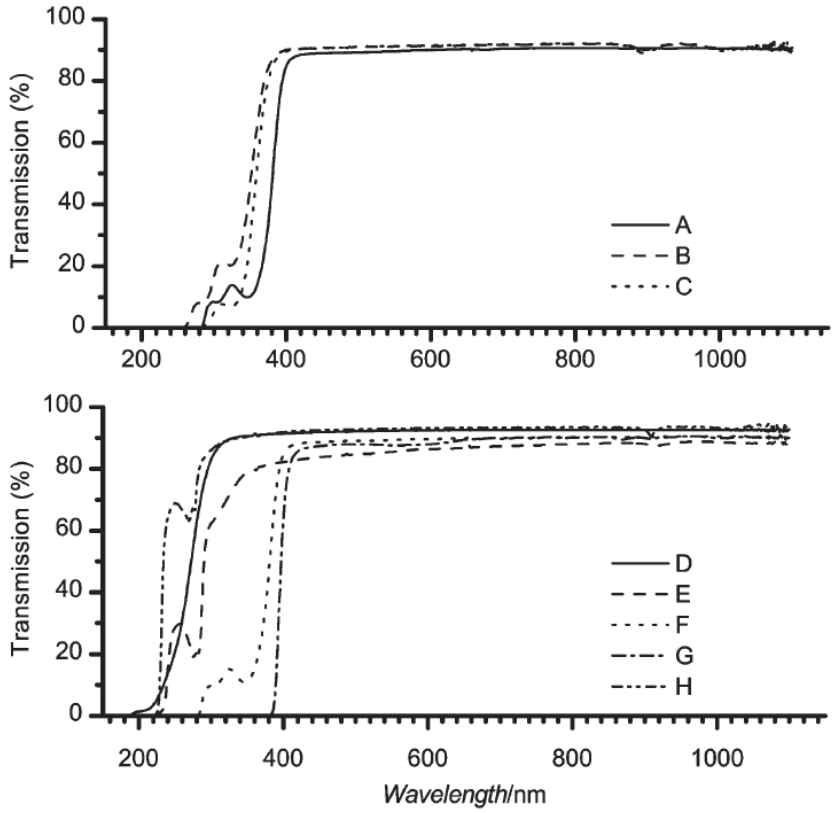

Figure 19: The transmission spectra taken at normal incidence of the plastic materials is shown. (A), (B) and (C) are spectra for various thicknesses of PMMA. On the bottom panel the materials are: (D) - Borofloat, (E) - Cyclic olefin copolymer (COC), (F) and (G) - various thicknesses of Poly carbonate (PC) and (H) - PDMS. This figure comes from from [40].

Refractive index matching

The similarity of absorption profiles between the quartz and the PDMS hints towards good refractive index matching between the two. This would be good as it would mean that the wavefront will keep its shape when focused by the BluRay lens (it is designed to focus 100μm into PMMA [41]). Also there will be less losses at the boundary. This turns out to be true since [42]:

$$n_{PDMS}(\lambda = 370\text{nm}) = 1.4537$$
$$n_{quartz}(\lambda = 370\text{nm}) = 1.4738$$

A sample that is built in the way described in this chapter means that there will be three optical surfaces to traverse, air to quartz (denoted aq), quartz to PDMS (denoted qp) and PDMS to air (denoted pa). For the light that touches a crystal there will be two more surfaces that include the interface between YSO and the PDMS. It is important to know the reflectivities of each surface to be able to understand the amount of lost light throughout the experiments. Using the Fresnel equation for reflectivity, i.e.,

$$R = \left|\frac{n_1 - n_2}{n_1 + n_2}\right|^2, \tag{9}$$

the reflectivities at the various interfaces will be: $R_{aq} = 0.037$, $R_{qp} = 4.7 \times 10^{-5}$ and $R_{pa} = 0.034$.

It should be noted that even though macroscopically the PDMS surface is bulged and rough, in the perspective of the focus, which is 1μm in diameter, the surface is flat. Therefore we expect about the same the same amount of light to be reflected at *aq* and *pa*.

Mounting process

The crystals were mixed into liquid PDMS at a given concentration to obtain about 70% surface area coverage when applied on the quartz. The mixture was then vacuum pumped in order to get rid of air bubbles which could act as scatterers in the sample. This mixture was then poured onto the quartz substrate and put into an oven at 80°C for about 30 minutes. Next time it might be interesting to spin coat the sample before it is put into the oven to make an even and thin surface of the mixture.

All in all a substrate made of quartz, with PDMS used as the adhesive polymer was optically the darkest way of mounting the microcrystals. It must also be mentioned that in the experiments, due to alignment issues (see Appendix G) the excitation light would enter the sample from the front of the quartz, denoted as the arrow in Figure 20. The same figure shows a schematic of the final sample.

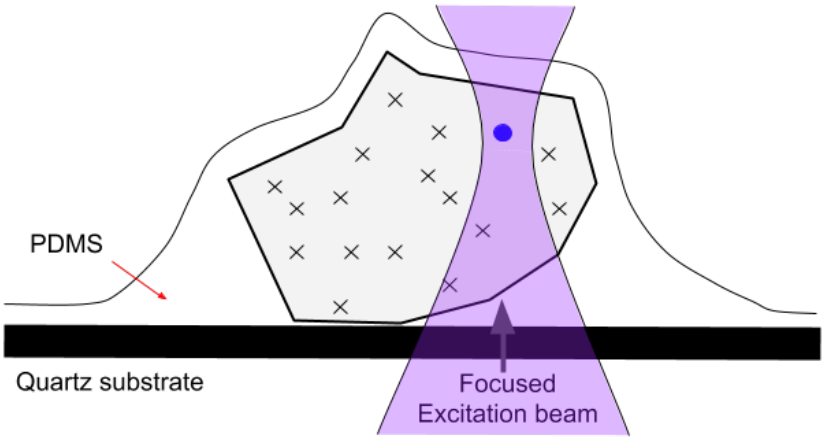

Figure 20: A schematic of the microcrystal on the substrate with the PDMS polymer surrounding it. According to measurements of the final sample the quartz plate is much thicker in real life, however, the point of the schematic is still valid.

5.3 Amendments to the holder

The holder, Figure 6, was made specifically for doing measurements on bulk crystals. In order for experiments on microcrystals to work, it has to be adapted so that one: the quartz plate along with substrate and microcrystals has to be mounted in a stable position and two: the background signal has to be decreased substantially in order even see fluorescence from microcrystals. The following sections will outline the work that has been done in these directions.

Suitable mounting

The fact that a bulk crystal was to be placed as the sample entails that a box to put it in along with some kind of blocking plate to lock it in place did a good job. However, in order to incorporate the imaging system from behind along with the mounting of a quartz plate in an upright position, some adjustments had to be made. Firstly, the back was cut off such that it is completely free for the imaging system to be able to image the whole plate. Secondly, a little groove was made in the bottom of the holder so that the plate could sit in a stable manner. The following figure shows the holder before and after the adjustments, although the groove is not included.

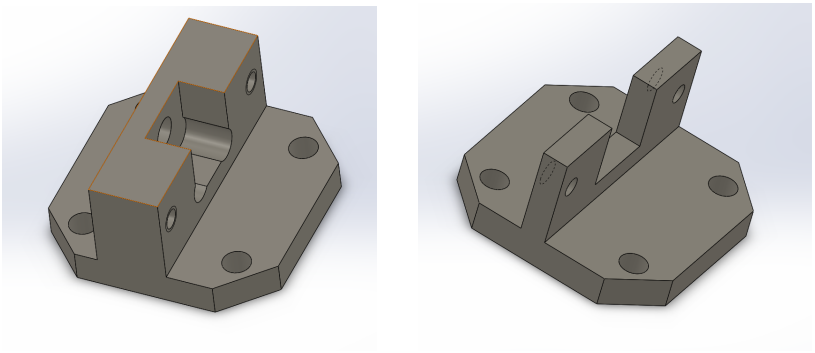

(a) Before modification (b) After modification

Figure 21: The crystal holder part before (a) and after (b) modification. The reason for doing this was to have the possibility of looking at the sample from behind.

Darkening the holder

Due to the high signal from bulk crystals, the fluorescence from the holder was never deemed a problem. It turns out that the plastic, polyether ether ketone (PEEK) that is the main material of the holder, fluoresces strongly under UV illumination. The spectrum is shown as the blue line in Figure 22.

This spectrum was taken at a temperature of 2.2 K, and it turns out that the intensity increases and the spectrum changes as one cools the sample down from room temperature. The reason for the increase in intensity could be due to the fact that it is an organic compound with a plethora of energy levels (rotational, vibrational and electronic). In room temperature many of these are populated by phonons so the molecules can deexcite nonradiatively. As the temperature decreases to superfluid helium temperatures phonons dissipate out of the sample without resistance forcing the molecules to deexcite radiatively! This is a significant hurdle as the signal from the PEEK is much higher than the signal from the microcrystals. Two ideas were tested, namely painting the PEEK with graphite paint or NEXTEL velvet coating 811-21 Schwarz paint. The spectra, under 370 nm illumination for one layer of the NEXTEL and graphite paint applied to PEEK, are depicted as the red and yellow curve of Figure 22 respectively (at 2 K). For illustrative purposes the spectrum using NEXTEL paint was zoomed in by an order of magnitude. As is obvious, NEXTEL paint eliminates the fluorescence from the PEEK most efficiently. The graphite paint on the other hand is

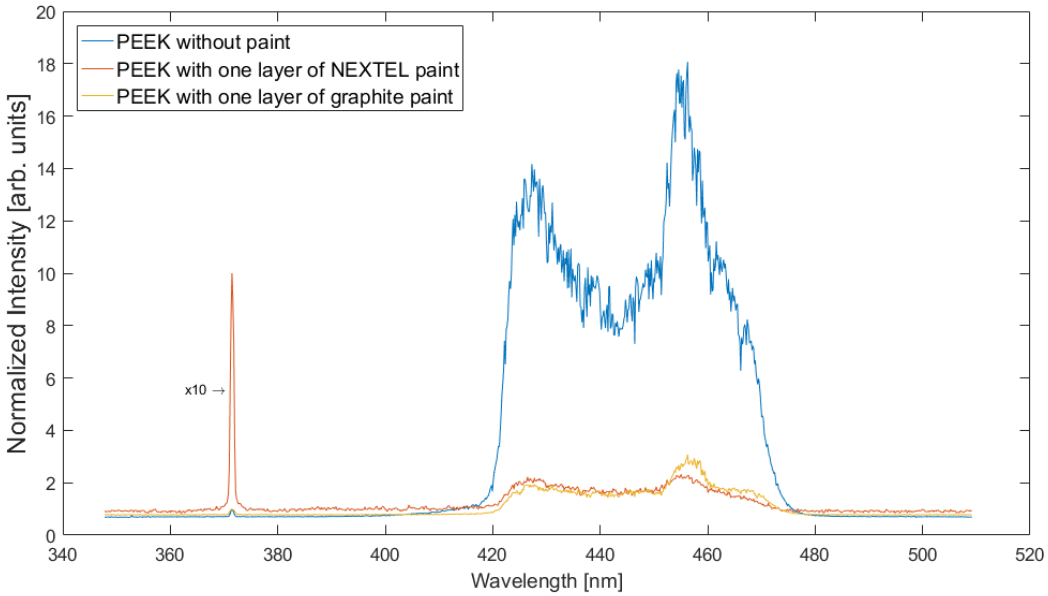

Figure 22: The spectra of PEEK, PEEK and NEXTEL paint and PEEK and graphite paint. The spectrum for the NEXTEL paint has been scaled by a factor of ten due to the low signal.

made out of graphite microspheres in water. When the water dries the microspheres remain stuck to the surface. This is probably the reason why it is not very efficient since it does not cover the PEEK completely, essentially working like a bad neutral density filter.

Another requirement for these paints is that it has to be possible to cycle in the cryostat without flaking. Figure 23 shows what the paints looked like before and after a couple cycles between room temperature and 2.2 K. One can see that the graphite paint has flaked off while, conveniently, the NEXTEL paint has not been affected.

(a) Before cycling (b) After cycling

Figure 23: The paints before and after cycling 5 times. The bottom layer corresponds to the NEXTEL paint and the upper layer to the graphite paint. One can see that the graphite paint has nearly completely disappeared.

From these conclusions and for good measure the holder was painted with four layers of NEXTEL paint.

5.4 Bulk crystal measurements at room temperature

Since wehad no feeling of the setup and we were aiming to understand why single ions had not been detected before, it was decided to optimize and characterize the setup by reproducing results from the bulk crystal. The crystal used had a concentration of 10^{-7}, a crystal with extensive documentation in [37] and [38]. Furthermore this was a good time to see a newly written raster scan in action (see Appendix H). It must also be noted that the expected fluorescence intensity was expected to be much lower than documented, as these measurements were performed in room temperature.

Spectrometer and SPAD comparison

The idea of these experiments is to see what size and type of signal one is to expect from the two detectors in the setup, and their interplay. Since we simply do not know what to expect from the microcrystals this is an important part of calibration that has to be done. Furthermore once there is a signal from the bulk crystal, optimizing the setup on it is an obvious choice over optimizing on nothing. Three experiments were performed after data collection optimization has been considered as in section 2.7. They are:

1. Reflecting the laser's light off a mirror placed by the sample and recording the signal on both the spectrometer and the SPAD.

2. Reflecting the laser's light off the surface of the bulk crystal and recording the signal on both the spectrometer and the SPAD.

3. Exciting the cerium ions within the crystal and collecting the fluorescence signal (after the longpass filter) in the spectrometer and SPAD.

If one is to integrate the spectrometer signals and divide them with the SPAD counts there will be a fixed factor that relates the two. This factor was found to be consistent between the laser reflected off the mirror and off the surface of the bulk crystal, however, it was a factor of one hundred lower when the comparison was made between the fluorescence signals. Initially it was thought to be due to the fact that the alignment was simply not good enough for the fluorescence to reach the SPAD (chromatic aberrations could play a larger role than expected). However, after many failed attempts of optimizing this, it was realized that the slit height of the spectrometer allowed a much larger number of photons to enter the spectrometer than the SPAD. This realization proved to be very useful when working with the microcrystals, since one can look for the signal on the spectrometer and then switch to the SPAD knowing how many photons to expect and vice versa.

A thorough characterization of the filters was also done during these experiments. They all work as they should!

Raster scan of the lens

Another experiment that was performed was to move the lens in steps towards the crystal and record the number of counts for each step along with the spectrum for some of the positions. The results are presented below.

The edge of the bulk crystal can easily be resolved when looking at (a), where the large step at about 5000μm corresponds to exactly this. In fact the derivative of (a) will give a measure of the depth resolution that one has with the SPAD [36].

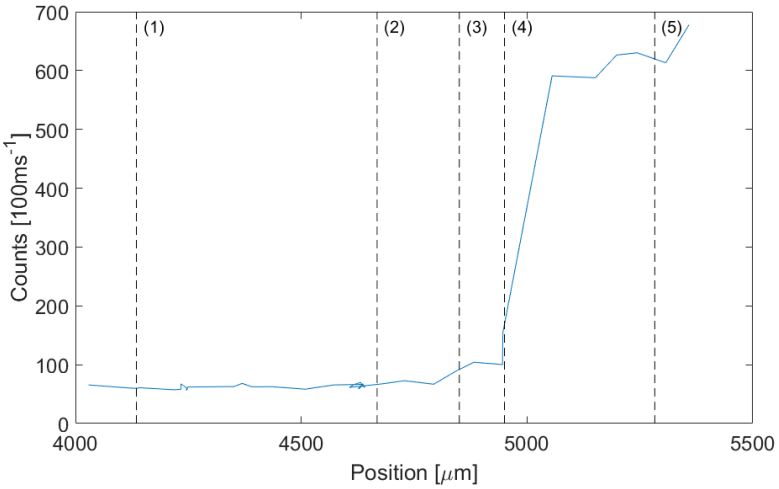

(a) The SPAD signal.

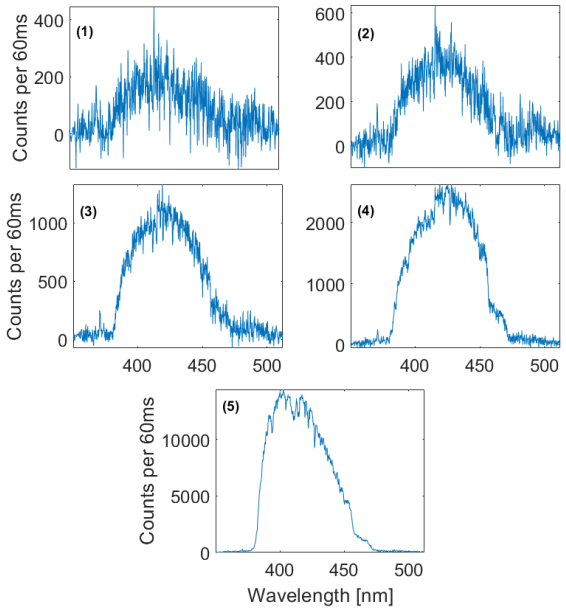

(b) The spectrometer signal.

Figure 24: Moving the lens towards the bulk crystal while counting fluorescence photons. The edge of the crystal can be seen with, in this case, a 30μm precision. The dashed lines in (a) correspond to the points at which the spectrum in (b) was measured.

If one runs this measurement through the pinhole simulation that has been previously described, the visibility of a spectrum on the spectrometer before the focus hits the crystal (Figure 24(b)) can be attributed to its larger slit height. Following is a figure of the simulated impulse response function of the spectrometer in the 1 cm slit length direction (a), and (b) shows the integrated spectra from Figure 24(b) as a function of the transmission given in (a).

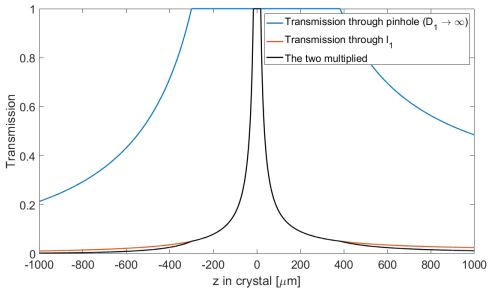

(a) The IRF of optical system using the spectrometer slit height.

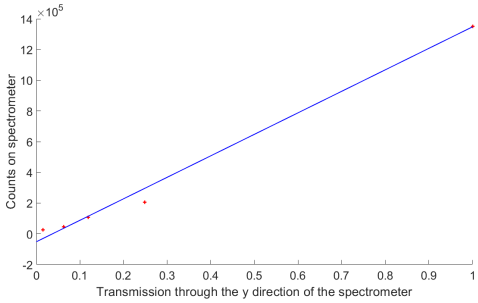

(b) The integrated number of counts from Figure 24 (b) as a function of the IRF at the corresponding position.

Figure 25: The simulation results of the system where the pinhole is set to be the spectrometer slit height along with the experimental results of spectrometer reading at various lens positions.

The linear results of Figure 25(b) validates the simulation as well as the statement that the spectrometer sees a larger volume. Also as a sidenote, it can clearly be seen in Figure 25(a) that the IRF is assymmetric as has already been discussed in previous sections.

Raster scan along the x-axis

The same experiment as above was performed for the x-axis. Here one can see a much less defined border between the crystal and air. This is attributed to the very sporadic nature of the x-attocube that did not work well during all the experiments. A more in depth discussion about this is included in Appendix E.

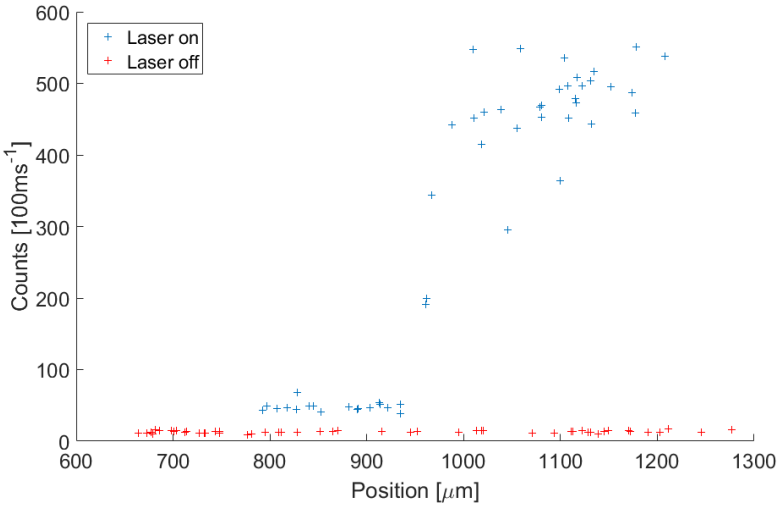

Figure 26: The results of the raster scan along the x-direction of the bulk crystal. It can be seen that the bulk crystal begins around 950μm, however, this border is not well defined due to the sporadic nature of the operation of the attocubes.

5.5 Microcrystal measurements at room temperature

The first measurements on microcrystals were performed at room temperature. Even though the amount of light coming from these would be much lower than at cryogenic temperatures, this downside was weighed out by the fact that one is easily able to fix things when working outside the cryostat. One can concentrate fully on understanding and pushing the limits of the system.

The sample measured optically

In order to see that everything works the way it should, the sample thickness was measured optically. It has already been mentioned that there will be some optical boundaries that we can identify with the reflection of the laser beam (section 5.2). Therefore the reflection intensity of the laser beam (without filters in place) while scanning the lens towards sample was recorded. This is done to see if the system is working, since all the thickness values and reflectivities should correspond to caliper measured values and theoretical values respectively.

It must be noted that this was done with very low intensity laser light due to the sensitivity of the single photon counter.

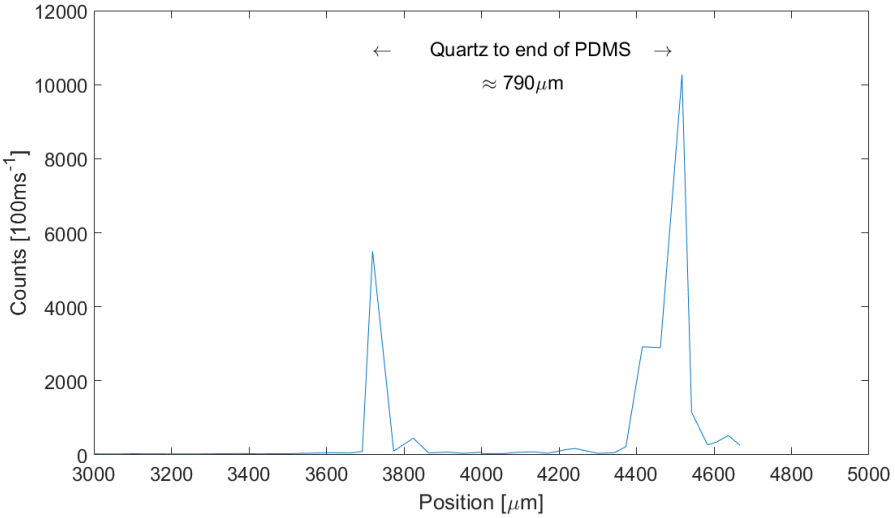

Figure 27: A raster scan in the z direction in order to optically characterize the size of the sample. It is in good agreement with the caliper measured size of (750μm).

Figure 27 is the result of exactly such a measurement. We can see two peaks corresponding to the air-quartz interface (the leftmost peak) and the PDMS-air interface (rightmost peak). The higher right peak, even though we have concluded that the two should be equal, is attributed to the fact that the the PDMS-air interface is not flat, hence reflections will come back from many directions simultaneously.

Background of 370 nm scattered light

A source of noise that was identified during the thesis work is the scattered excitation light along the excitation beam path, especially within the black detection box itself. After all, the excitation light coming out of the experimental fiber has a relatively high power. To measure this a beam dump was placed at the position of the sample and the light was turned on and off 1400 times. The blue curve in Figure 28(a) corresponds to when the laser is turned off while the red curve corresponds to the laser turned on and led into the beam dump. Figure 28(b) depicts the mean of the two signals along with the standard deviation of the mean.

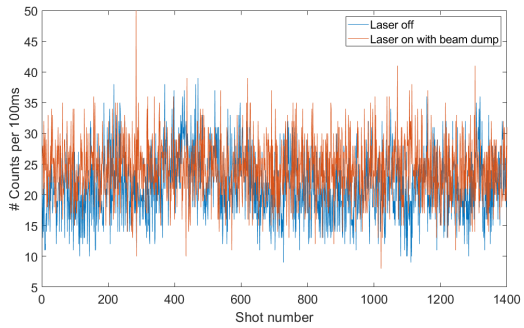

(a) Raw data of 1400 shots at a given position.

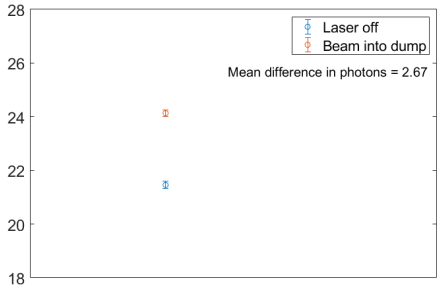

(b) Mean values of (a).

Figure 28: The first shots at a random position on the sample. We see a difference between the on and off signal which is due to scattered excitation light.

As is shown in Figure 28(b) the signal coming from scattered laser light is about 3 photons per 100 ms higher than the dark counts.

Since the expected signal from microcrystals and single ions is so low, the stray scattered light within the box was deemed an issue. Therefore, in order to get rid of it, another black shield was placed in the box further enclosing the SPAD. To be fully sure, the longpass filter was placed right in front of the SPAD so that any light that hits it is above 380 nm.

Raster scan in the y direction

This section presents the scan along the y axis when the first microcrystals were detected. There are two figures below: the attocube readout to show that the scan is fully stable and the final processed data where each point corresponds to the number of counts per 100 ms at a given position.

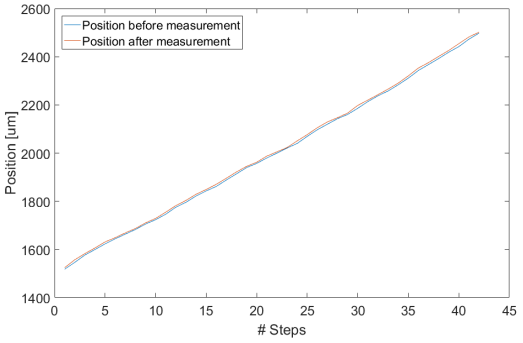

(a) The position readout before and after measurement of the y axis attocube as a function of step number.

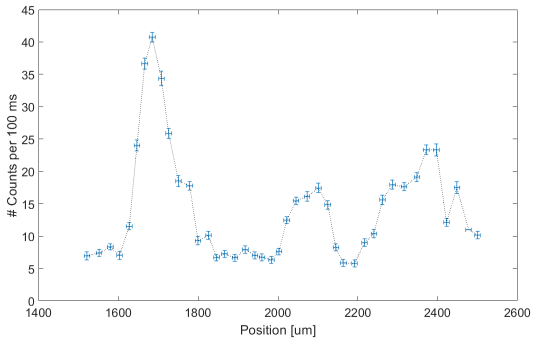

(b) The final processed data from the scan in the y-direction.

Figure 29: A scan of the attocubes in the y-direction along with photon counts of the fluorescence. The error bars in the number of counts of (b) represent the standard deviation of the mean of the shots, while the error bars in the x-direction correspond to the attocube error taken as the difference between the blue and red line in (a).

One can see in Figure 29(a) that the attocubes move in an extremely stable manner, something that was unique for the y-attocube throughout this thesis work. If one compares to the results from the x-scan in Figure 26, it is obvious that this stability is very important for a successful measurement with high spatial resolution. When it comes to Figure 29(b), each point is the average of 75 consecutive 'laser on/laser off' measurements meaning that at a given position the laser is turned on then off 75 times. The counts from the laser off measurement at that point (corresponding the the dark counts of the SPAD) are subtracted, setting a background level to about 6 photons per 100 ms.

Spectra at various points in y

Spectra were then taken at different positions of Figure 29(b). The following two are examples of this where (a) is taken at the center of the highest peak, i.e., at 1700μm and (b) in between the first and second peak at 1920μm.

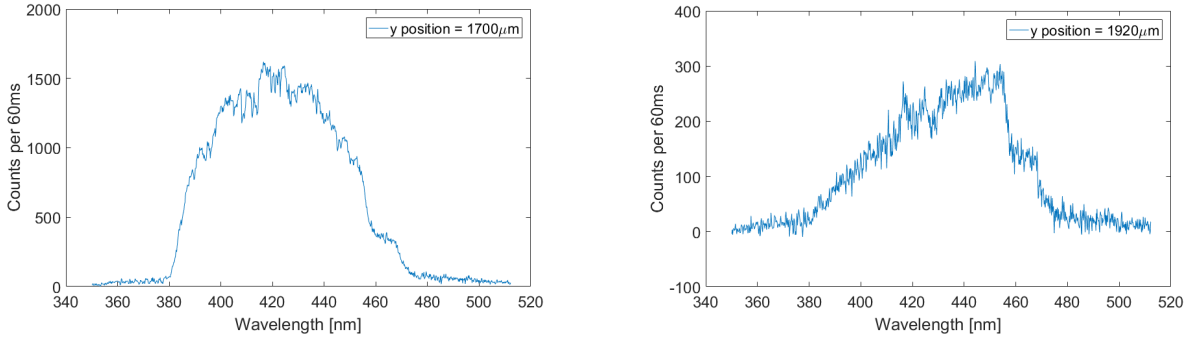

(a) Taken at $y_{pos} = 1700\mu$m.

(b) Taken at $y_{pos} = 1920\mu$m.

Figure 30: Spectra taken at various positions on the crystal. The spectrometer has a higher collection volume than the single photon detector.

We can see that in the peak (Figure 30(a)), the spectrum corresponds to a very well defined room temperature cerium spectrum (a) (figure 8.3 of [38]), while at the background level (b), a different spectrum can be seen. The high wavelength side, i.e., between 450 and 480 nm, looks quite similar to the cerium spectrum of (a), however, at lower wavelengths it is not recognizable as cerium or, for that matter PEEK. It is not sure where this spectrum comes from. An attempted explanation attributes this to the larger slit size of the spectrometer that might collect better at higher wavelengths. A promising fact is that its intensity is much lower!

Since a lot of work has been put into understanding the signal differences between the SPAD and the spectrometer and numerically characterizing their interplay, a comparison between the two signals was made in the following figure:

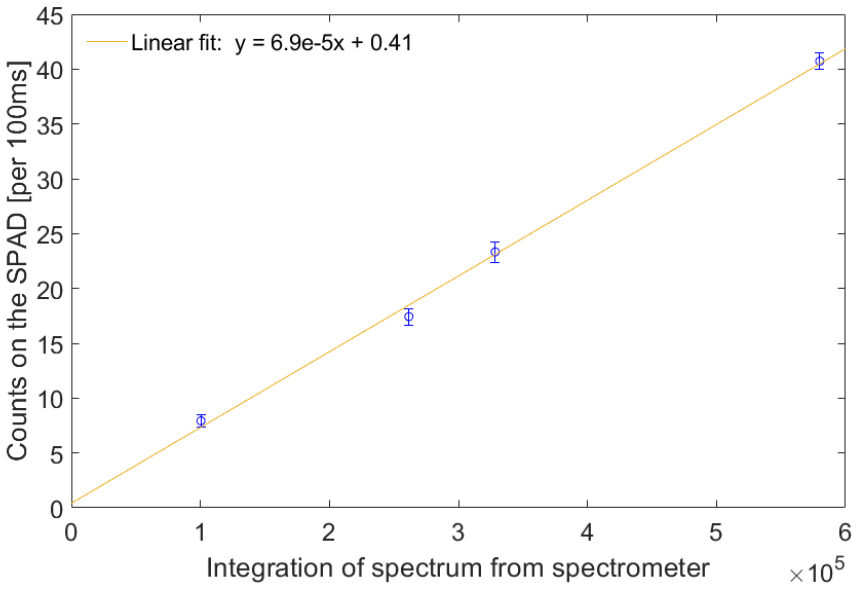

Figure 31: A comparison between the number of counts off the SPAD and the integrated spectrum of from the spectrometer. The first point corresponds to the zero between the first and second peak of Figure 29(b) and the others correspond to a peaks in the same figure

The SPAD signal was plotted against the integrated number of counts on the spectrometer. The high linearity between the two goes to show that none of the detectors are saturated and the readout parameters of the spectrometer and SPAD were chosen correctly. Furthermore it is settling to see that even the background signals at y_{pos} fit the linear relation.

5.6 Microcrystal measurements at cryogenic temperatures

After having obtained a good grasp of the measurement system, the microcrystals were lowered into the cryostat for experiments at 2.2 K. The bulk crystal was not included on the sample holder for these measurements.

Microcrystal spectrum

Following is a spectrum of cerium in a single microcrystal with the theoretical energy structure for cerium.

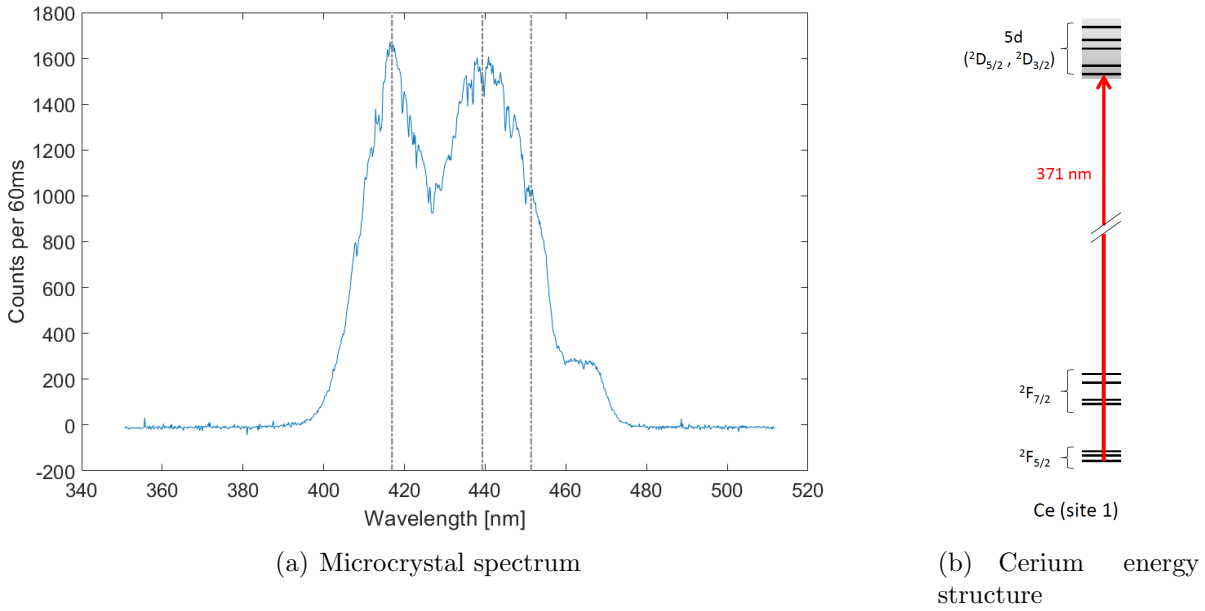

(a) Microcrystal spectrum

(b) Cerium energy structure

Figure 32: A spectrum of a single microcrystal where the dashed lines correspond to peaks that are comparable to those in the literature for bulk crystals. (b) shows the energy structure of cerium used in the text in order to explain the lines of (a).

The dashed lines of Figure 32(a) correspond to the position of some important peaks that can be compared to in the literature. Their values here are: 416.9 nm, 439.3 nm, 451.4 nm. The corresponding peaks in literature are: 402 nm, 425 nm, 440 nm (page 83 in [37]) and are attributed to the 4f $^2F_{5/2}$ - 5d transition, the lower two Stark levels in the 4f $^2F_{7/2}$ - 5d transition and the upper two Stark levels in the 4f $^2F_{7/2}$ - 5d transition respectively. The reason behind the offset of about 15 nm in all the collected microcrystal spectra as compared to those of bulk measurements is unknown. Initially it was thought that a calibration mistake was the culprit, however, upon calibrating the spectrometer with a mercury spectral lamp, it turned out that indeed, the calibration was correct. Furthermore this only happens at cryogenic temperatures since we see from Figure 30(a) that the signal experiences the characteristic increase at 380 nm, just like in literature.

During this thesis work, 3 - 4 single microcrystals were investigated and they all had this identical spectrum.

Inhomogenous profile

The following figure is mainly an attempt at spectrally turning the cerium signal off rather than the inhomogenous profile, however this term will be used nonetheless. The center wavelength, i.e., 0Hz detuning, was set as 370.84 nm ([37] and [38]).

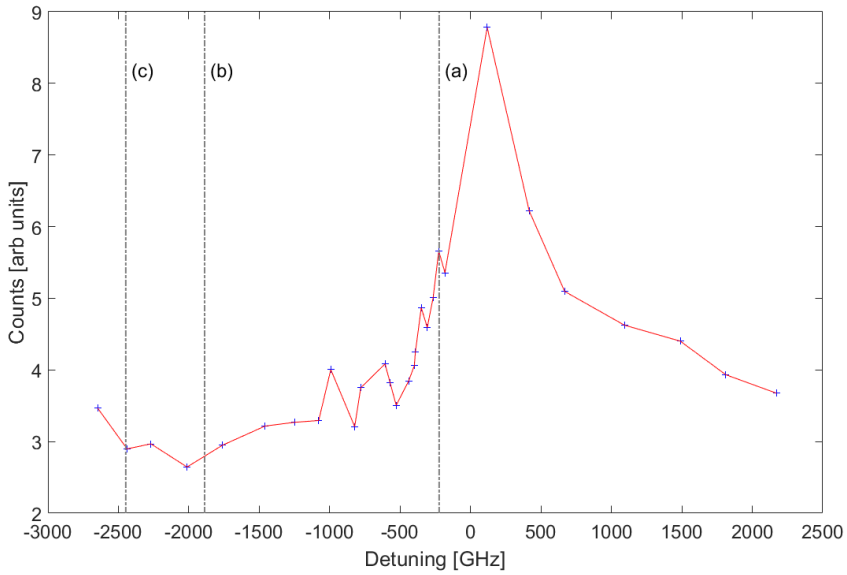

Figure 33: The measured inhomogenous profile of a microcrystal. The grey dashed lines correspond to positions where the spectra of the next figure were taken.

This measurement, where the red line is only there to connect the data points, is mostly inconclusive. It is much wider than the reported 37GHz, however, not enough points were taken within this range to be sure about this. This inconclusiveness and will to spectrally turn the cerium signal off, led to the recording of spectra at different detunings, denoted as the dashed lines (a), (b) and (c) of Figure 33. Cerium can occupy two different positions in the unit cell named site 1 and site 2. These will have slightly different spectroscopic properties [38] where site 2 fluoresces at higher wavelengths (negative detunings). In order to make sure that cerium site 2 fluorescence would be blocked at the lower detuning positions, the bandpass filter was included for these measurements. Following are these spectra:

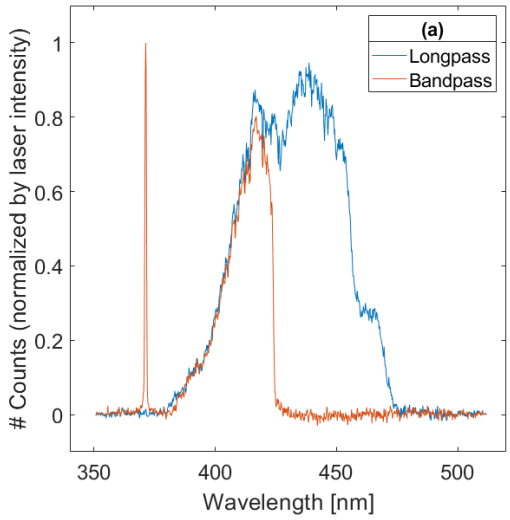

(a) -233GHz detuning

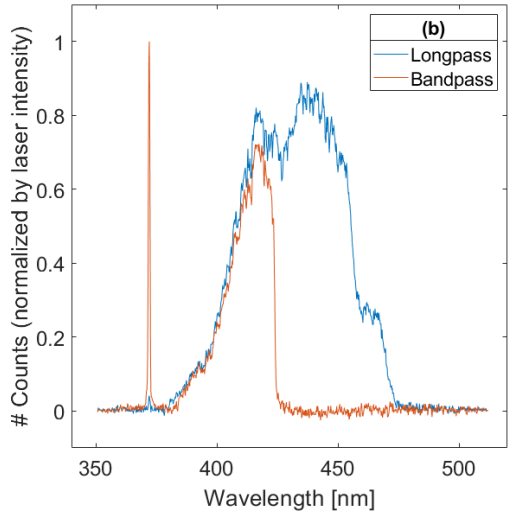

(b) -1888GHz detuning

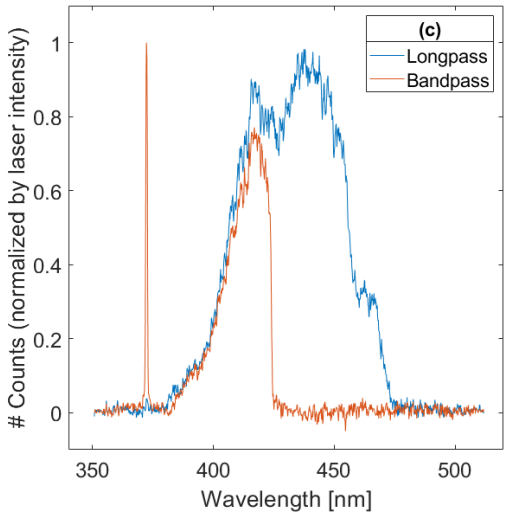

(c) -2447GHz detuning

Figure 34: The spectra using a longpass and bandpass filter at various detunings, attempting an explanation of the width of the inhomogenous profile in Figure 33.

The spectra of Figure 34 are normalized to the red laser line that comes through the bandpass filter. The reader will notice that the spectra are all cerium site 1 spectra, with no site two signals whatsoever and they all have close to the same intensity. There are three explanations to this, either we are indeed in a regime of single ions and this is the signal from them, the inhomogenous line broadened to a high degree for some non-apparent reason or the homogenous linewidth is boradened. More measurements are necessary in order to draw further conclusions.

5.7 Experiments on a single microcrystal

Due to structural instabilities in the holder and mirrors before the cryostat, it proved to be quite difficult to find and then work with one single microcrystal for a longer period of time. However, on one of the lab days this was indeed possible.

Microcrystal size

It was observed that one could move on and off the microcrystal in all three axes, so the size of it was examined in that way. Following is a figure taken when scanning the attocubes in all three directions. The small discontinuities in these figures are attributed to the slip and stick mechanism of the attocubes.

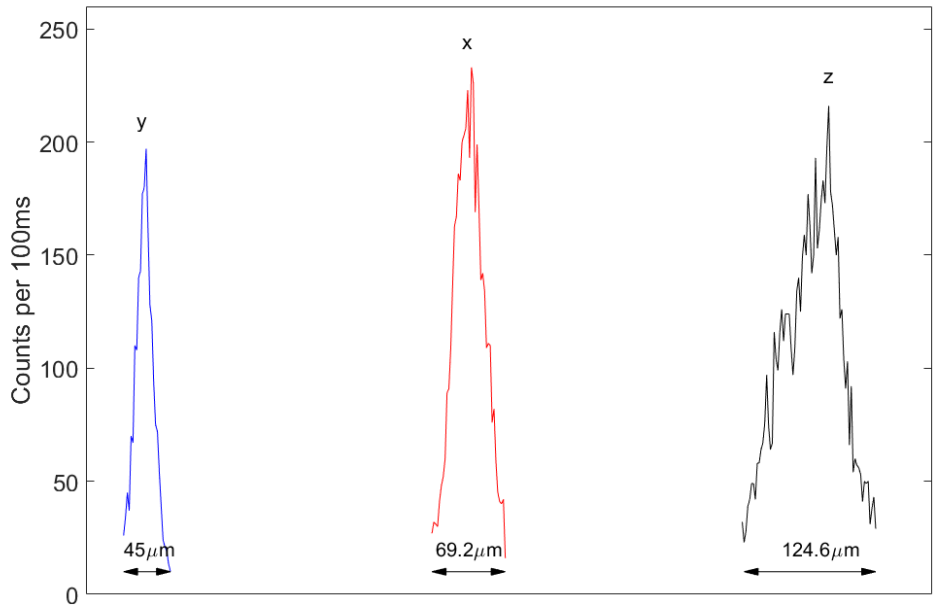

Figure 35: A scan over the crystal in all three axes, the x, y and z direction. The jumps in the signal are attributed to the slip and stick mechanism of the attocubes.

By reading the feedback from the attocubes the size of the crystal in each axis could be extracted (marked under the curves). It must be noted that the feedback of the x and z attocube did not work properly so the sizes were measured by recording the time it took to go over the crystal, then calibrated with the well functioning y direction. These values correspond to the axes that go through the center of the crystal. If one moved the focus to the side of the crystal closest to us (moving the focus as far back as possible) and scanned over y the value was instead 29μm while it was 60μm at the back. By doing this in all three axes it would in principle be possible to record the exact shape of this crystal with an accuracy corresponding to the accuracy of the confocal setup and the attocubes. This was however not performed since other measurements were deemed more relevant.

Saturation intensity

Information about the fluorescence intensity from the microcrystals is necessary to evaluate the losses in the system and also get an understanding about when we have reached a single ion. Furthermore one can look look at the fluorescence intensity from the background (where there is a possibility of reaching a two photon process) and work in a regime where the difference between the cerium fluorescence and background fluorescence is at its highest. Following is a figure illustrating this exact measurement where the background was taken 5μm away from the crystal.

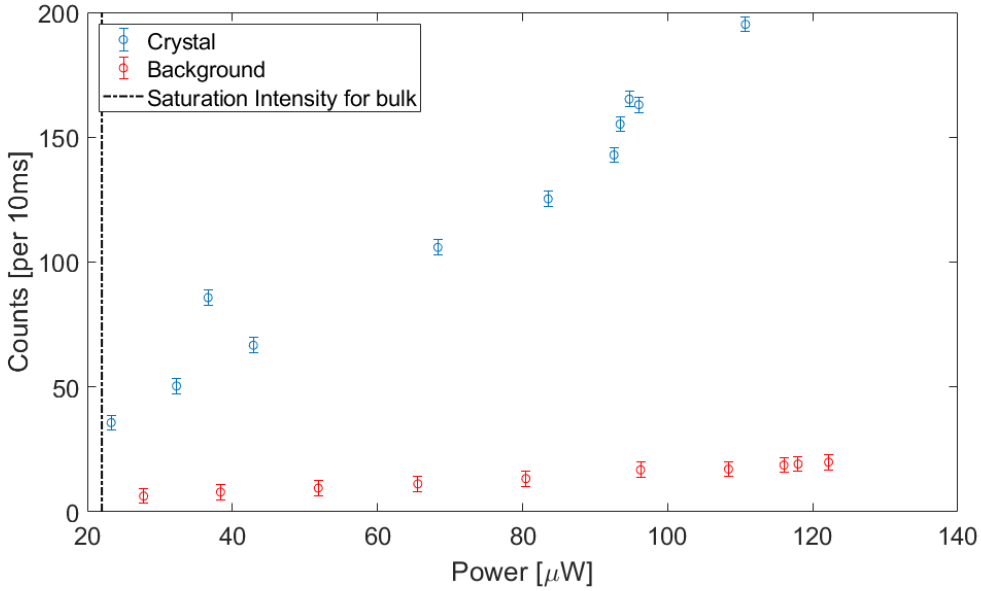

Figure 36: A plot of the number of counts on the SPAD as a function of excitation intensity. The blue plot was taken in the middle of the crystal, i.e., in the middle of all three lines in Figure 35. The red line, was taken 5μm above the crystal. The errorbars represent an upper limit of the number of dark counts, 3 counts per 10 ms.

The saturation intensity of cerium is 1.4×10^7 Wm^{-2} which, given the focal length and size of the BluRay lens, corresponds to an input power of 15μW. The transmission of the cryostat windows is about 70%, so this corresponds to a power of about 22μW before the cryostat. The black dashed line in Figure 36 corresponds to this point. As is visible, the fluorescence intensity (in blue) keeps going up way past the dashed line, indicating that no where near that much light reaches the cerium within the crystals. Moreover this increase cannot be attributed to the background intensity either since the red line stays quite flat all the way.

In principle one could calculate the losses of the sample by looking at the slope of the blue curve and assuming that the number of photons hitting the detector at saturation will be around 10^5 s^{-1} (as previously discussed in section 2.6). However, seeing that there seems to be huge losses of the excitation light along the way, there will be just as many losses for the fluorescence coming back, so the number of photon counts at saturation is rather uncertain now!

Other measurements

Other measurements on this crystal included trying to see what the inhomogenous profile looks like. The results were just as inconclusive as in Figure 33. Spectra were also taken at various detunings and again the same results were achieved, i.e., cerium site 1 spectra could be seen at high detunings. The spectrum of this crystal was also identical to Figure 32 with the equivalent 10nm shift of the structure.

5.8 Homogenous linewidth

Since we see that the light does not turn off at high detuning it was interesting to know if the homogenous line was still narrow enough to be able to use the proposed readout scheme. Therefore it was decided to try to do some Zeeman hole burning.

There are two things to be considered. Firstly the orientation of the crystal's axes is random compared to the magnetic field, and along the b-axis of the YSO crystal the splitting has been reported to be 19 MHz/mT [26]. However, there is no reference as to how the crystal b-axis relates to the cerium g-tensors. Despite this, since the largest cerium g-tensor ($g_2 = 2.319$) is 5 times higher than the smallest ($g_1 = 0.545$) [43], in the worst case scenario we will split the levels five times less than in the reported 19MHz/mT (see Equation 2). Considering Figure 36, and an excitation power of 38μW that was used during the experiments, the light that hits the cerium is considerably lower than in the bulk experiments so hole burning will not be as efficient.

The first experiments were performed exactly as in [26], i.e., burning a hole at $\Delta\nu = 0$ for 300μs then scanning over a range of 200 MHz for 100μs. The following figure shows the results at three different fields, where the shape of the curve at no field (blue circles) corresponds to the acousto-optic modulator (AOM) efficiency curve.

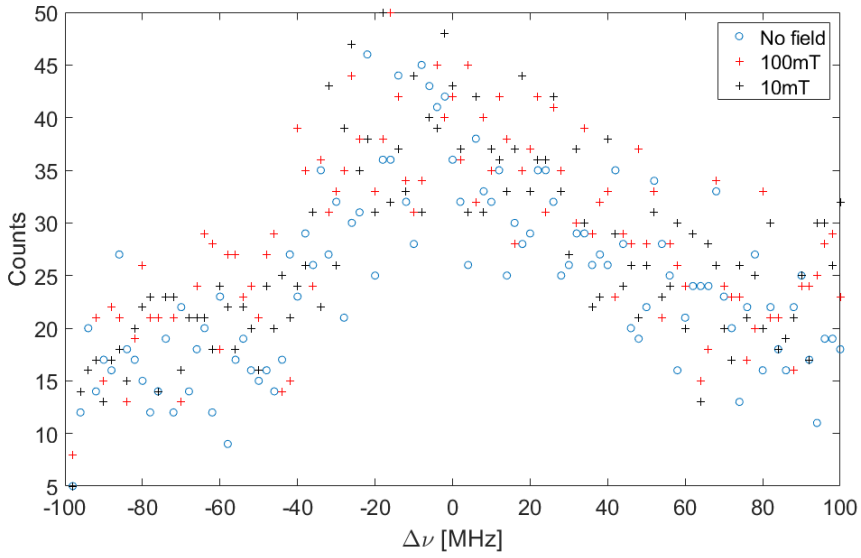

Figure 37: The result of the readout scan after hole burning for 3 different magnetic fields.

As can be seen the zero difference between the points for a magnetic field and no magnetic

field means that we were not able to burn a hole. With Figure 36 in mind, it was concluded that there might not have been enough laser power on the crystal after all. In hindsight one could have simply increased the burn pulse length in time.

Instead it was decided to burn continuously at two frequencies, separated by 140 and 160 MHz while slowly increasing the magnetic field strength. If we were to burn a hole at these two frequencies, the fluorescence counts would initially decrease (because we are burning holes in each group of atoms) and then at some point in the magnetic field ramp, the Zeeman splitting will correspond to the frequency separation between the pulses, bringing a peak into sight. At this point we will be burning the atoms back and forth between their Zeeman levels! Following is a figure of those experiments and as can be seen, there is nothing there.

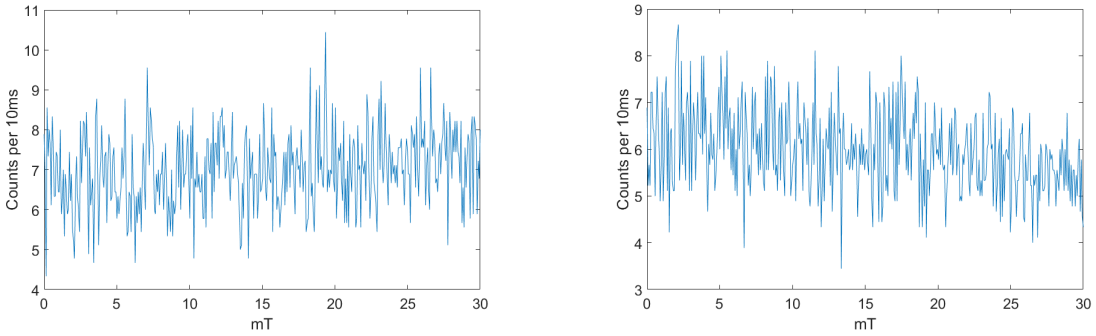

(a) $\Delta\nu = 140$ MHz (b) $\Delta\nu = 160$ MHz

Figure 38: Counts as a function of magnetic fields while undergoing constant burning with a frequency difference of 140 and 160 MHz respectively. The magnetic field was ramped from 0 to 30 mT over five minutes.

6 Conclusion

All in all, the successful detection of single microcrystals has led to the possibility of performing spectroscopic measurements on these small structures and probably bringing us considerably closer to single ion detection and manipulation.

There are however some basic questions remaining such as, is the inhomogenous profile actually that wide? Why is the spectrum shifted by ten nanometers? Are other properties of cerium the same as in bulk? In principle the large size of these crystals should mean that most of cerium dopants are in a bulk like environment, however, these measurements do hint towards the fact that we should be prudent with this assumption.

Maybe soon the detection of a single cerium ion will be performed in microcrystals and a real readout protocol will be executed, paving the way for single instance quantum computing!

Acknowledgements

I have now spent two years with the quantum information group, a new home within the physics department. I would like to thank the whole group for the fun times and great atmosphere I was a part of throughout my thesis projects. I would like to give a special thanks to Adam Kinos who was my first supervisor and inspiration when I wasn't sure what I wanted to do. The answer turned out to be really easy, but you had to be there to show me. Then Sebastian Horvath and Chunyan Shi for spending a really great three weeks in the lab together and always being ready to have either fun or serious discussions with me! Also Ying Yan, for the time spent with me before the summer of 2018, it was a great week of lab work together. Then I would like to thank Ivan Scheblykin for the help with the substrates and Mats Andersson for the NEXTEL paint. Also Eric Andersson for helping me out with the spectrometer, I hope you had a good time in the lab! I've since heard rumours that you want to scratch your position to become an experimentalist? The biggest thanks goes to Stefan Kröll who is always ready to listen and then discuss anything with me! You have been a great mentor for the end of my education and I really feel like these two years have been the most stimulating and rewarding in my education, mainly thanks to the trust, help and freedom you have given me.

References

[1] Andrew Steane. Quantum computing. *arXiv:quant-ph/9708022*, Aug 1997.

[2] Michael A. Nielsen and Isaac L. Chuang. *Quantum Computation and Quantum Information*. Cambridge University Press, Cambridge, UK, 10th anniversary edition, 2000.

[3] David P. DiVincenzo. The physical implementation of quantum computation. *quant-ph*, 2000.

[4] Vassily Kornienko. Sensitivity of various qubit detection methods in pr:y2sio5., 2017. Some of the paragraphs in the introduction were directly copied from this thesis.

[5] Austin G. Fowler, Matteo Mariantoni, John M. Martinis, and Andrew N. Cleland. Surface codes: Towards practical large-scale quantum computation. *Phys. Rev. A*, 86:032324, Sep 2012.

[6] Janus H. Wesenberg, Klaus Mølmer, Lars Rippe, and Stefan Kröll. Scalable designs for quantum computing with rare-earth-ion-doped crystals. *Phys. Rev. A*, 75:012304, Jan 2007.

[7] M. R. Drout, A. L. Piro, B. J. Shappee, C. D. Kilpatrick, J. D. Simon, C. Contreras, D. A. Coulter, R. J. Foley, M. R. Siebert, N. Morrell, K. Boutsia, F. Di Mille, T. W.-S. Holoien, D. Kasen, J. A. Kollmeier, B. F. Madore, A. J. Monson, A. Murguia-Berthier, Y.-C. Pan, J. X. Prochaska, E. Ramirez-Ruiz, A. Rest, C. Adams, K. Alatalo, E. Bañados, J. Baughman, T. C. Beers, R. A. Bernstein, T. Bitsakis, A. Campillay, T. T. Hansen, C. R. Higgs, A. P. Ji, G. Maravelias, J. L. Marshall, C. Moni Bidin, J. L. Prieto, K. C. Rasmussen, C. Rojas-Bravo, A. L. Strom, N. Ulloa, J. Vargas-González, Z. Wan, and D. D. Whitten. Light curves of the neutron star merger gw170817/sss17a: Implications for r-process nucleosynthesis. *Science*, 2017.

[8] Dennis Upper. The unsuccessful self-treatment of a case of "writer's block". *J. Appl. Behav. Anal.*, 7:497, 1974.

[9] Adam Kinos, Qian Li, Lars Rippe, and Stefan Kröll. Development and characterization of high suppression and high entendue narrowband spectral filters. *Appl. Opt.*, 55(36):10442–10448, Dec 2016.

[10] Mahmood Sabooni, Qian Li, Lars Rippe, R. Krishna Mohan, and Stefan Kröll. Spectral engineering of slow light, cavity line narrowing, and pulse compression. *Phys. Rev. Lett.*, 111:183602, Oct 2013.

[11] Qian Li, Yupan Bao, Axel Thuresson, Adam N. Nilsson, Lars Rippe, and Stefan Kröll. Slow-light-based optical frequency shifter. *Phys. Rev. A*, 93:043832, Apr 2016.

[12] Lars Rippe, Mattias Nilsson, Stefan Kröll, Robert Klieber, and Dieter Suter. Experimental demonstration of efficient and selective population transfer and qubit distillation in a rare-earth-metal-ion-doped crystal. *Phys. Rev. A*, 71:062328, Jun 2005.

[13] L. Rippe, B. Julsgaard, A. Walther, Yan Ying, and S. Kröll. Experimental quantum-state tomography of a solid-state qubit. *Phys. Rev. A*, 77:022307, Feb 2008.

[14] A. M. Dibos, M. Raha, C. M. Phenicie, and J. D. Thompson. Atomic source of single photons in the telecom band. *Phys. Rev. Lett.*, 120:243601, Jun 2018.

[15] Tian Zhong, Jonathan M. Kindem, John G. Bartholomew, Jake Rochman, Ioana Craiciu, Varun Verma, Sae Woo Nam, Francesco Marsili, Matthew D. Shaw, Andrew D. Beyer, and Andrei Faraon. Optically addressing single rare-earth ions in a nanophotonic cavity. *Phys. Rev. Lett.*, 121:183603, Oct 2018.

[16] E. Petersen L. Renn A. Götzinger S. Sandoghdar V. Utikal, T. Eichhammer. Spectroscopic detection and state preparation of a single praseodymium ion in a crystal. *Nature Communications*, 5:3627, 2014.

[17] Roman Kolesov, Kangwei Xia, Rolf Reuter, Mohammad Jamali, Rainer Stöhr, Tugrul Inal, Petr Siyushev, and Jörg Wrachtrup. Mapping spin coherence of a single rare-earth ion in a crystal onto a single photon polarization state. *Phys. Rev. Lett.*, 111:120502, Sep 2013.

[18] G.F. Imbusch B. Henderson. *Optical Spectroscopy of Inorganic Solds*. Oxford University Press, Oxford University Press - New York, 1st edition, 1989.

[19] John G. Bartholomew, Rose L. Ahlefeldt, and Matthew J. Sellars. Engineering closed optical transitions in rare-earth ion crystals. *Phys. Rev. B*, 93:014401, Jan 2016.

[20] Samuel Bengtsson. Simulation and modeling of rare earth ion based quantum gate operations, 2012. Master Thesis.

[21] A. Walther, L. Rippe, Y. Yan, J. Karlsson, D. Serrano, A. N. Nilsson, S. Bengtsson, and S. Kröll. High-fidelity readout scheme for rare-earth solid-state quantum computing. *Phys. Rev. A*, 92:022319, Aug 2015.

[22] Ying Yan, Jenny Karlsson, Lars Rippe, Andreas Walther, Diana Serrano, David Lindgren, Mats-erik Pistol, Stefan Kröll, Philippe Goldner, Lihe Zheng, and Jun Xu. Measurement of linewidths and permanent electric dipole moment change of the ce $4f$-$5d$ transition in y_2sio_5 for qubit readout scheme in rare-earth ion based quantum computing. *Phys. Rev. B*, 87:184205, May 2013.

[23] Diana Serrano, Yan Ying, Jenny Karlsson, Lars Rippe, Andreas Walther, Stefan Kröll, Alban Ferrier, and Philippe Goldner. Impact of the ion-ion energy transfer on quantum computing schemes in rare-earth doped solids. *Journal of Luminescence*, 151:93–99, 02 2014.

[24] Y. Kharitonov N. Belov Maksimov B, V. Ilyukin. Crystal structure of yttrium orthosilicate. 183:1072–1075, 1968.

[25] Weerapong Chewpraditkul, Chalerm Wanarak, Tomasz Szczesniak, Marek Moszynski, Vitezslav Jary, Alena Beitlerova, and Martin Nikl. Comparison of absorption, luminescence and scintillation characteristics in luysio5:ce,ca and y2sio5:ce scintillators. *Optical Materials*, 35(9):1679 – 1684, year = 2013, issn = 0925–3467.

[26] Jenny Karlsson, Adam N. Nilsson, Diana Serrano, Andreas Walther, Philippe Goldner, Alban Ferrier, Lars Rippe, and Stefan Kröll. High-resolution transient and permanent spectral hole burning in ce^{3+} : y_2sio_5 at liquid helium temperatures. *Phys. Rev. B*, 93:224304, Jun 2016.

[27] Thomas Kornher, Kangwei Xia, Roman Kolesov, Nadezhda Kukharchyk, Rolf Reuter, Petr Siyushev, Rainer Stöhr, Matthias Schreck, Hans-Werner Becker, Bruno Villa, Andreas D. Wieck, and Jörg Wrachtrup. Production yield of rare-earth ions implanted into an optical crystal. *Applied Physics Letters*, 108(5):053108, 2016.

[28] Andrew J.S. McGonigle David ". Coutts. Cerium-doped fluoride lasers. *IEEE Journal of Quantum Electronics*, 40:1430, 2004.

[29] Mike Hodges. Single photon avalanche diodes, 2014.

[30] Frederick R. Chromey. *To Measure the sky*. Cambridge University Press, University Printing House, Cabridge, 2nd edition, 2016.

[31] Phil C. D. Hobbs. *Building Electro-Optical Systems - Making It all Work*. John Wiley Sons Inc, Hoboken - New Jersey, 2nd edition, 2009.

[32] Jenny Karlsson, Lars Rippe, and Stefan Kröll. A confocal optical microscope for detection of single impurities in a bulk crystal at cryogenic temperatures. *Review of Scientific Instruments*, 87(3):033701, 2016.

[33] Xingqiu Zhao. Diode laser frequency stabilization onto an optical cavity, 2013. Master Thesis.

[34] Eric D. Black. An introduction to pound–drever–hall laser frequency stabilization. *American Journal of Physics*, 69(1):79–87, 2001.

[35] Lars Rippe. *Quantum computing with naturally trapped sub-nanometre-spaced ions*. PhD thesis, Lund University, 2006.

[36] Tony Wilson. *Confocal Microscopy*. Academic Press Limited, 1 edition, 1990.

[37] Jenny Karlsson. *Cerium as a quantum state probe for rare-earth qubits in a crystal*. PhD thesis, Lund University, 2015.

[38] Ying Yan. *Towards single Ce ion detection in a bulk crystal for the development of a single-ion qubit readout scheme*. PhD thesis, Lund University, 2013.

[39] Sune Svanberg. *Atomic and Molecular Spectroscopy*. Springer Verlag, 4 edition, 2004.

[40] A. Piruska, I. Nikcevic, S.H. Lee, C. Ahn, and W.R. Heineman. The autofluorescence of plastic materials and chips measured under laser irradiation. *Lab Chip*, 5:1348, Nov 2005.

[41] BluRay Disc Association. White paper, blu-ray disc^{TM} format, 2015.

[42] refractiveindex.info. A database for the refractive indices of common materials.

[43] M Buryi, V.V. Laguta, Dariya Savchenko, and M Nikl. Electron paramagnetic resonance study of lu2sio5and y2sio5 scintillators doped by cerium. *Advanced Science, Engineering and Medicine*, 5:1–4, 06 2013.

[44] Shbyrnes321. Wikimedia commons file: Ray transfer matrix definitions, 2016.

Appendix

A Miscellaneous observations

There were some observations that were not of major importance to this thesis however when the next person moves towards single ion detection, these should be considered.

A.1 The fiber collimator

A beam analyzer was put in immediately after the collimator for the experimental fiber on the experimental table (i.e., before the 10/90 beamsplitter on the top left of Figure 8), and Figure 39 is the result. It is easy to see that this is not a very nice Gaussian beam!

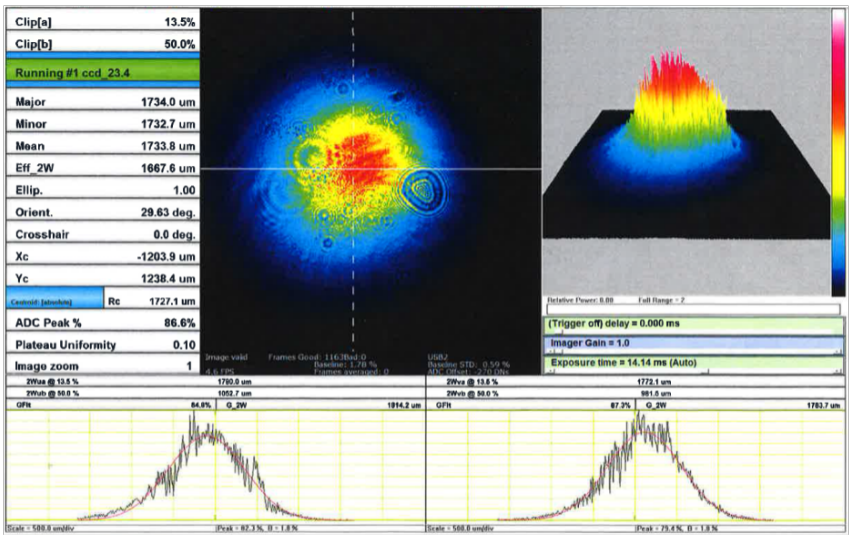

Figure 39: The collimated beam right after the fiber collimator for the experimental fiber. This is before it has touched any optics whatsoever.

The fringes on the beam shape indicate some clipping of the beam after it comes out of the fiber. This is not a problem for the confocal imaging of the system through the pinhole, since the fluorescence is incoherent. However such a distorted beam shape will introduce abberations in the focusing of the light into the crystals. This means firstly, that the focus will not be as tight, and secondly, the intensity of the light on the single ion may fluctuate with spatial vibrations of the system, in turn lowering the fidelity of the readout mechanism. An easy fix is to change the fiber collimator model.

A.2 Crystal far at the back of the PDMS

There was a time when I was on a crystal and I wanted to look at its size in the z-direction. However, the reflection from the back of the PDMS ended up overshadowing the fluorescence. The following figure shows this. The crystal starts at step number 20. The crystal should

end at the dashed line since this point corresponds to the 4500 mark of Figure 27. This is of course problematic since this crystal cannot be used for experiments. A way to solve this would be to put a quartz plate in the back, to refractive index match on the boundary.

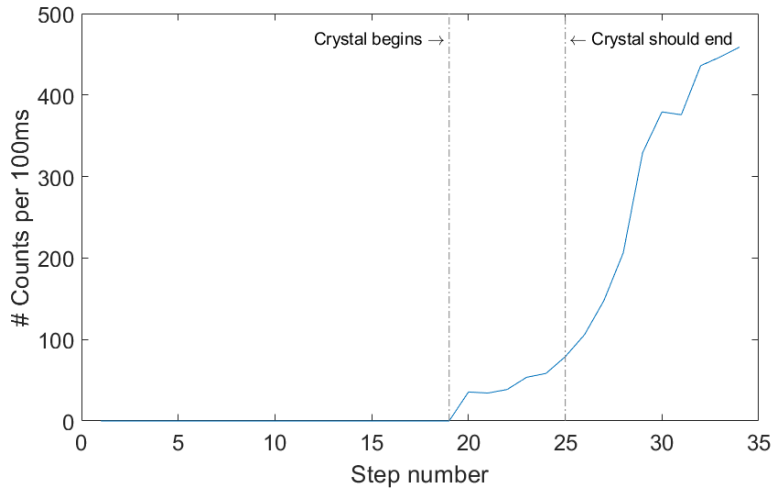

Figure 40: A z-raster scan where the first increase in counts corresponds to a crystal and the rest (behind the second dashed line) corresponds to reflections off the PDMS. Each step is about 10 microns long.

B Characterization of the setup

For the purpose of documentation the laser power at various points on the laser table was documented however. These values correspond to when the laser works well taken with the laser servo supplying 71.4 mA and at a wavelength of 370.8561 nm

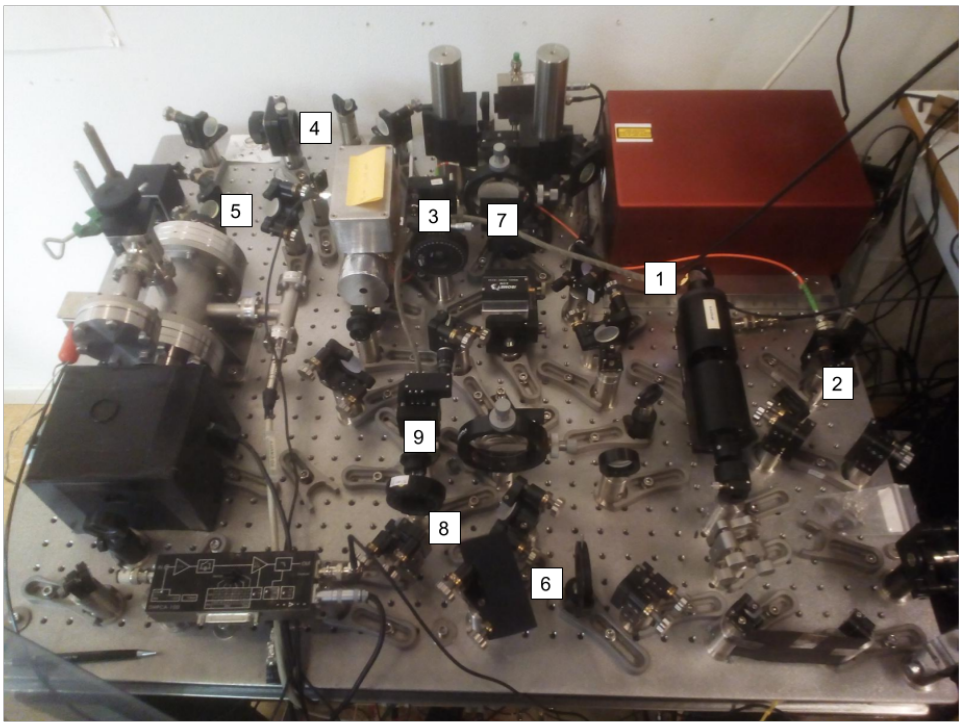

Figure 41: The numbers on this figure correspond to positions where the laser power was measured and these are displayed in the following table.

Position	**Power [μW]**
1	11 100
2	1909
3	214
4	102
5	93
6	4662
7	204
8	977
9	710

Table 2: A table of the powers at different positions on the table. It is important to note that the powers were taken using an Ophir powermeter which is only specified to go down to 400 nm. Using the responscurve for the meterhead, a factor of 4.44 was retrieved to multiply the readout value with and convert to the real power at 370 nm. These values are written in this table.

C Laser Locking characteristics

During the project [33] was used thoroughly as documentation. Here is a section which lists everything the experimentalist needs to know for good locking and pulse shaping. Some values might deviate from the documented ones from day to day, however these will give a ballpark!

Electro-optical modulator (EOM) documentation

This short section gives the documentation for the parameters that give the maximum modulation depth for the laser locking

- Frequency and phase from the DDS
  - + EOM frequency: 20.175 MHz
  - + Phase difference: 11966 (see DDS manual for how to convert this number to an angle)
- EOM amplifier driving power: 24 V and 2.667 A

Oscilloscope readings for locking

Note that these readings were taken with the DHCPA-100 detector at a step lower than maximum gain.

Letter	Height (mV)
a	50
b	205
c	60
b/a	24.3%

Figure 42: The oscilloscope reading for successful locking. The ratio in the bottom of the table indicates the best modulation depth that was achieved.

Cavity characterization

Following is a figure of the transmission profile of the cavity followed by a figure of the ringdown time. The fits are Lorentzian and exponential respectively. These experiments were performed by Sebastian Horvath and deviate from the previously documented linewidths, due to a vacuum leak!

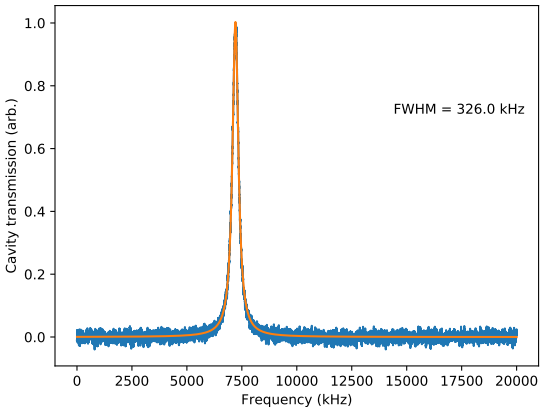

Figure 43: A lorentzian fit to the cavity transmission, with a FWHM of 326 kHz.

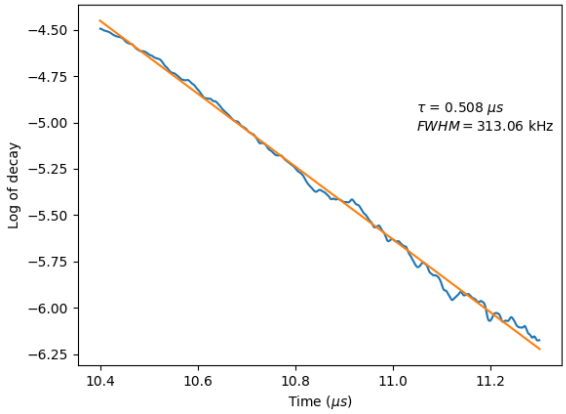

Figure 44: The cavity ringdown, fitted with an exponential, giving a FWHM of its corresponding Lorentzian 313kHz

Acousto-optic modulator (AOM) documentation

The maximum driving power as written in the manual is 0.450 W at our wavelength, however we drove it at 1 W. This is not a problem as it is specified to be able to work that far!

D The detection setup

For the purpose of documentation a picture of the detection setup (i.e., the parts in the black dashed box of Figure 8) is included in Figure 45. The blue arrows represent the excitation laser beam and the purple represents the fluorescence coming back from the sample, i.e., identical color coding to Figure 8.

Outline of the detection setup

The light comes to the setup from the laser table via an optical fiber, marked as the first blue arrow in the bottom right corner. It then hits two mirrors that are used for the alignment onto the dichroic mirror (c) which in turn reflects the excitation light out of the box. Care must be taken that the dichroic mirror has a 45° tilt, as it is at this angle that the coating works best. Moreover it is important that the light coming out of the box after point (c) is collinear with all the optics on the other side (shown in the figure as the purple arrow to the left of point (c)). This will make the alignment of the fluorescence onto the detectors much easier. The detectors are the SPAD, (a) and the spectrometer (b). The pinhole was not used in the experimental work of this thesis since the size of the active area of the SPAD offers enough depth discrimination for work with the microcrystals. It is excluded in the picture.

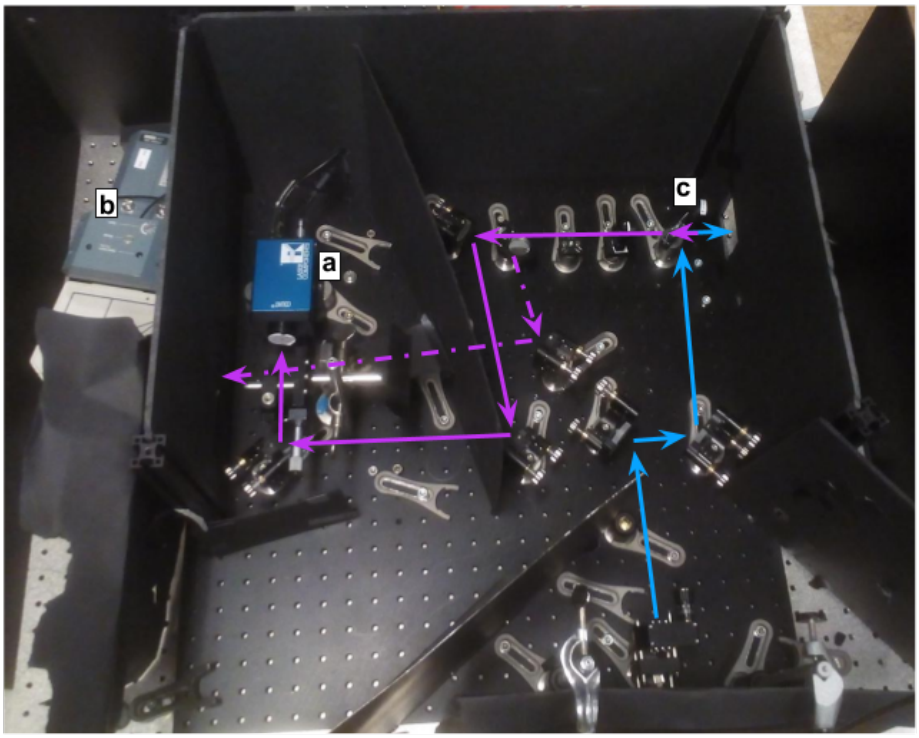

Figure 45: A real picture of the detection setup. (a) is the Single Photon Counter, (b) is the Spectrometer and (c) is the dichroic mirror followed by the two filters to the left. The colour coding is such that the blue arrow correspond to the excitation light and the purple arrows correspond to the fluorescence light.

The components and their relevant parameters

- **Spectrometer**
  The spectrometer is from Oriel Instruments, model number: 77400 equipped with an Andor Technology DH501-25U-01 CCD camera. The parameters used for the CCD for optimized measurements are: exposure time = 0.06 s and gain = 9. The accumulation then depends on how low the signal is, but could be anything between 2000 and 15000 shots! The grounding time was also set to 0.06 s, however this is a parameter that could have been further optimized for better measurements. The spectrometer has a slit size of 1 cm $\times 100\mu$m.

- **Single Photon Counter**
  The Single Photon counter is a Laser Components Count Blue 250B with a dark count rate of 250 per second and a 45% detection efficiency at 370 nm. The active area of this detector is $100 \times 100\mu$m.

- **Dichroic mirror**
  The dichroic mirror, a Semrock BrightLine FF380-Di01 has a reflection band (where reflection is above 95%) between 350 and 375 nm. The transmission band is between 385 and 450 nm. This will be important for explaining some of the spectra later on.

- **Filters**
  To the left of the dichroic mirror in Figure 45 there are two filters. One is a bandpass filter while the other is a longpass filter. The bandpass filter's transmission band is between 383 and 425 nm (Chroma/ET405) efficiently removing fluorescence from cerium site 2 and could be useful for bringing β down to 1.15. The longpass filter transmits above 380 nm. These are both interference filters so the angle at which they are placed will play a major role in their attenuation efficiency.

E Attocube Problems

It was noticed during this thesis work that the stepping function of attocubes did not work as they were supposed to. It is either the readout mechanism that is unreliable or the actual stepping that is unreliable. Even with a LabView program that is supposed to move the attocubes within a given error the following figure shows the complete unreliability of the posititioners.

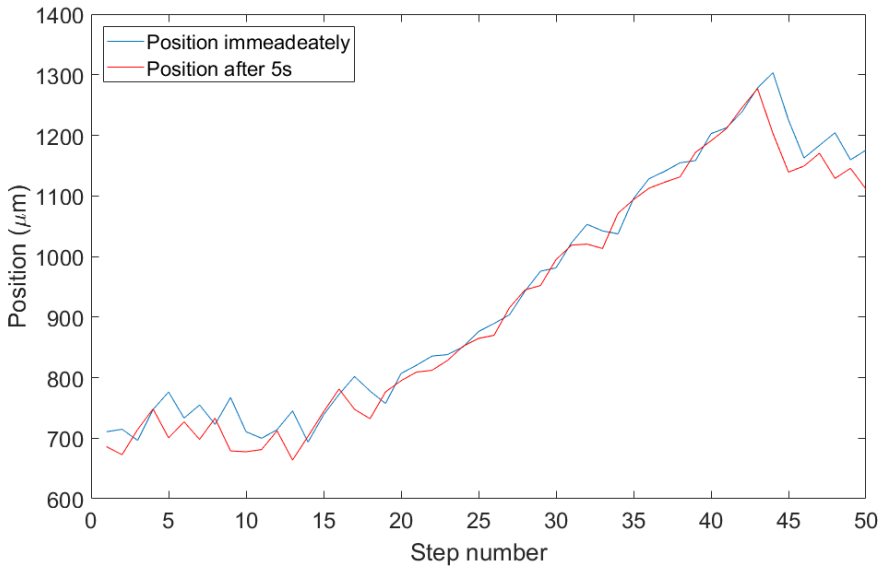

Figure 46: The position as a function of step number during the x raster scan at room temperature on bulk. This explains the lack of an edge in Figure 26.

This problem has been discussed a lot and comes mainly from the x-attocube. The reasons could range from unbalanced mounting to wires or pieces snagging on the positioners as they move. It could also be that the attocubes are stepping properly but the readout is unreliable. All in all, the way to figure this out would be to put them on a table with no extra wiring and check if they are up to specifications in stability and readout. If this is inconclusive a Michelson interferometer setup can be built in order to check if the readout is faulty or if the stepping mechanism is faulty.

The cabling going into the cryostat should also be considered and fixed since this would often break in multiple places.

F List of improvements to the experiment

This appendix gives the reader a list of the things that are deemed necessary to fix before the next round of experiments. Everything has already been discussed in the thesis, however a document where everything is listed with references to sections gives an easy way to see what is going on

- Attocube feedthrough wiring (section 3.2 and Appendix E.)
- Attocube feedback characterization (section 3.2 Appendix E).)
- Paint closer to the lens due to scattering onto the PEEK and introduction of background signal.
- Accurate mirrors in front of cryostat to make sure the beam position is reproducible. (Section 5.7)
- Mechanical way of adding filters and flipping the spectrometer mirror remotely. This is because every time these things are performed there is a risk of hurting the alignment.
- Stability of the holder that works after cycling many times. It was seen that the holder pieces became slightly loose after many weeks of experiments. Thought must be put into how to ensure the stability of it!
- Thinner quartz plate in front of the PDMS and microcrystals since it was noticed that the lens would hit the quartz before focusing at the back of the sample was achieved. With respect to Appendix A.2 a quartz plate should be added to the back of the sample.
- Controlled regions of varying surface density of the microcrystals for various measurements. For example, looking at the inhomogenous line could be done with a more dense microcrystal powder while single ion detection has to be done on a single microcrystal.
- Add the bulk sample in some good way, maybe glue it to the back of the quartz plate
- Look into the fiber collimator on the experimental table, Figure 39.
- Look into the quartz that is used and spin coat the sample (with reference to section 5.2.)
- Mode match the light into the experimental fiber in the same way that Chunyan and Sebastian have done on the 606 laser system. They have basically fully characterized the beam before the fiber and added optics in order to obtain high coupling efficiency!
- It has been recommended by Jenny Karlsson that we should change the BluRay lens to a lens similar to that which they have in Paris. Adam knows more!

G Alignment process

It is important to align the system such that the light gathered in the focus of the BluRay lens is collimated and then sent all the way back into either the spectrometer or the SPAD. For the purpose of documentation the alignment process is included in this section:

1. Put a mirror as far away from the fiber as possible such that the reflected beam is exactly collinear with the incoming beam. If one wants to be really careful one can make sure that the beam comes back out of the fiber on the laser table. Usually it is enough to be as close as one can before the fiber. This way some of the reflected beam (at 370 nm) will go through the dichroic mirror into the detection setup, pictured as the purple line in Figure 45.

2. The filters, mirrors and lenses after the dichroic mirror are then to be aligned until the signal on either detector is maximized! This makes sure that any beam that comes out of the sample exactly the same way that it went in will hit the detectors.

3. The mirror that reflects the beam should then be taken out of the setup so that the light goes through the BluRay lens onto the sample. The light that then touches the surface of the sample will not always come back the same way it came in, since there is an unknown tilt on the sample. The fluorescence signal size will also change for two reasons, namely one: this tilt will decrease the efficiency of getting the light in under the surface to the ions and two: the seven degree solid angle of fluorescence that is accepted by the system might decrease. Since we are looking at really low signals, this could make a difference. Therefore it is important that the light coming onto the sample is perpendicular to it. This can be done my moving the focus back and forth until the circle of reflection increases and decreases in diameter symmetrically around its point of smallest diameter. The two mirrors before the cryostat can be tweaked to obtain this result.

H Raster scan

Since the imaging system did not quite work the way we wanted it to work, a raster scan program was developed. Here is the schematic of the way it is organized:

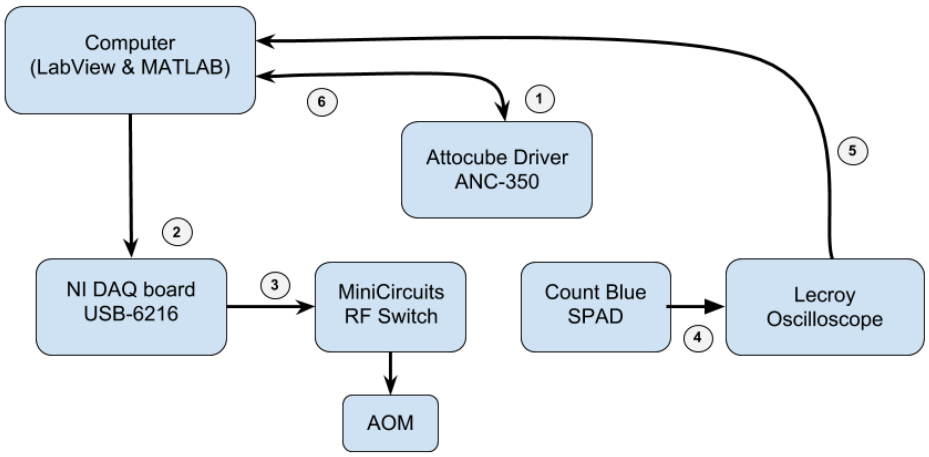

Figure 47: The Raster scan schematic where the numbers give the order of events. In true LabView spirit the arrows point in the data flow directions.

The steps went as follows:

1. The attocubes are stepped in a given direction. When the stepping is over, the program enters a loop that has the purpose of stepping the attocubes back and forth until they are at the desired position plus minus a certain tolerance. The position is then read out and saved.

2. With the attocubes in place, a data acquisition (DAQ) board is told by the computer to create a digital transistor-transistor logic (TTL) output signal.

3. This TTL signal switches an RF signal on, which is then lead to an acousto-optic modulator (AOM). Only the first order beam goes through the fiber onto the table, so this works as a fast on/off switch.

4. The single photon detector starts detecting and the LeCroy oscilloscope, triggered by the LabView program, collects the number of counts.

5. This number of counts is then sent via ethernet to the computer where it is stored in a text file.

6. The attocube position is read again, to find out if the sample had moved during the measurement.

I Spatial hole burning

The following figures are figures of the permanent hole burning in the spatial dimension. This is where the approximate value of 5μm spatial FWHM of the permanent hole come from. These experiments were performed by Adam Kinos.

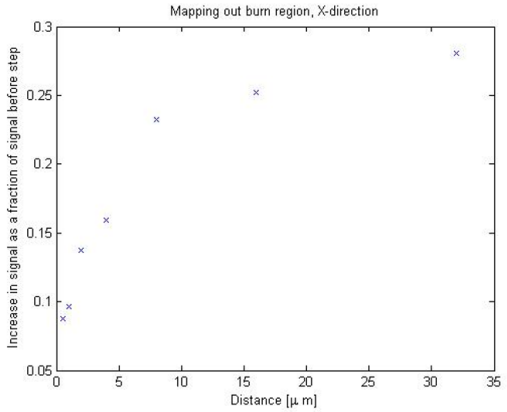

(a) Hole burning in x.

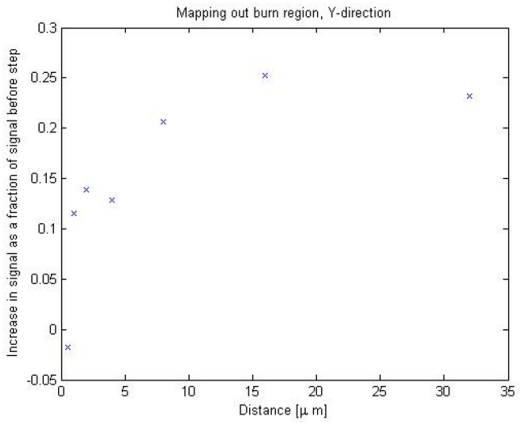

(b) Hole burning in y.

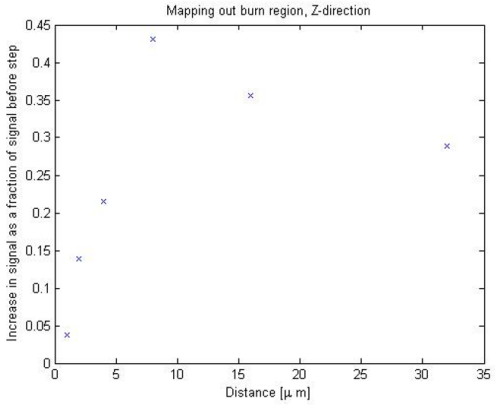

(c) Hole burning in z.

Figure 48: Hole burning with spatial position dependence. The fluorescence signal seems to come back at about 15μm for every dimension!

J Ray transfer matrix analysis

Ray transfer matrix analysis is an efficient technique to analyze and trace light rays as they pass through optical components. This easy technique works because in the geometrical approximation, an optical component operates linearly on a light ray. A light ray is fully defined by its height (x) and angle (θ) at which it propagates with respect to the optical axis. One can collect these values in a 2 by 1 matrix where the first element is x and the second element is θ.

An optical component, defined as a plane perpendicular to the optical axis can be represented as a 2 by 2 matrix that operates linearly on the ray matrix. Hence the propagation of the light ray that is shown in Figure 49, through an optical component (shown as a lens in the same schematic) can be described by the following equation:

$$\begin{pmatrix} x_2 \\ \theta_2 \end{pmatrix} = \begin{pmatrix} A & B \\ C & D \end{pmatrix} \begin{pmatrix} x_1 \\ \theta_1 \end{pmatrix} \tag{10}$$

For more than one optical component one simply multiplies Equation 10 with the components' ABCD matrix from the left.

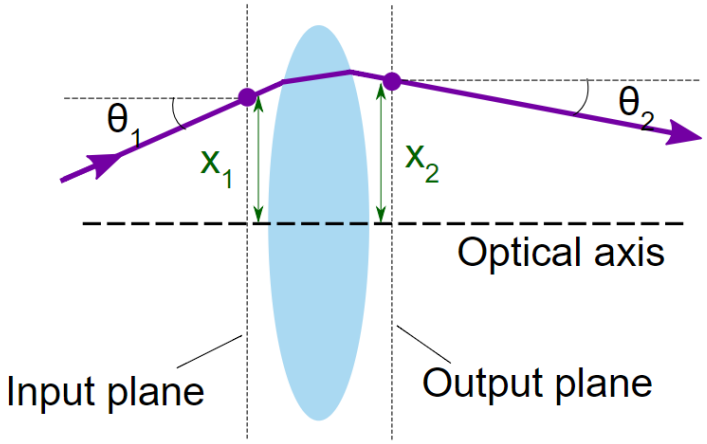

Figure 49: A schematic of the ray matrix method. Figure taken from [44]

Two ABCD matrices that represent the optical components used in the simulation are:

Propagation a distance d through free space: $\begin{pmatrix} 1 & d \\ 0 & 1 \end{pmatrix}$

A thin lens of focal length f: $\begin{pmatrix} 1 & 0 \\ -\frac{1}{f} & 1 \end{pmatrix}$